

ESA STUDY CONTRACT REPORT –**Deliverable D 5.2****Final simulation and testing guidelines**

ESA Contract No: 400114452/15/ NL/NDe	SUBJECT: D 5.2 Final simulation and testing guidelines	CONTRACTOR: Riga Technical University, Institute of Materials and Structures
* ESA CR()No:	No. of Volumes:1 This is Volume No:1	CONTRACTOR'S REFERENCE: 62518 (bidder code)
<p>ABSTRACT:</p> <p>A current report summarises a set of guidelines derived from extensive effort on setting up the numerical and analytical analysis procedures. All developed numerical procedures or analytical or based on finite element method were verified analytically and validated with experimental tests. Moreover as summary of best practice concerning experimental investigations and specimen preparations are covered within current report. All numerical analysis was implemented by commercial finite element software code ANSYS by scripting APDL log files. Where main emphasis was focused on barely visible damage (BVID) introduction by indentation and estimation of residual dent depth and accumulated damage in honeycomb and composite structure. While numerical methods capture all variety of boundary conditions, lay-up and honeycomb orientation as well as geometrical and material non-linearities, the analytical approach assumes symmetry and equivalent load distribution around dent. Both analytical tool verification and finite element model (FEM) validation was performed in line with series of physical experiments. Finally we have achieved good correlation among dozen of currently tested specimens by assessing residual indentation (barely visible damage BVID) and prediction of load carrying capacity of compression after impact tests (CAI), which are uploaded on project web page under section of SIV and CAIV (www.bnm4eks.rtu.lv).</p>		
<p>The work described in this report was done under ESA Contract. Responsibility for the contents resides in the author or organisation that prepared it.</p>		
<p>Names of authors: Oļģerts Ozoliņš; Kaspars Kalniņš; Guntis Japiņš; Eduards Skuķis; Jānis Andersons, Gints Jēkabsons.</p>		
<p>** NAME OF ESA STUDY MANAGER: DIV: DIRECTORATE:</p>	<p>** ESA BUDGET HEADING:</p>	

Table of contents

Introduction	5
1 General consideration in development of numerical model	6
1.1 Numerical model development strategies for finite element method	6
1.2 Element type assumptions	9
1.2.1 Shell element SHELL 281	9
1.2.2 Solid element SOLID186.....	10
1.2.1 Contact interface elements.....	12
1.3 Material models.....	14
1.4 Validation of lamina failure criteria.....	21
1.5 Boundary conditions and loading.....	23
1.6 Mesh sensitivity analyses	25
1.7 Plasticity model sensitivity analyses.....	27
1.8 References	27
2 Verification and validation of numerical approach.....	28
2.1 Validation of numerical models based on Indentation (IND) experiments 28	
2.2 Validation of numerical models based on CAI experiments	30
2.3 Numerical model comparison with tested panels	39
3 Analytical model of residual indentation upon low-velocity impact of a sandwich panel.....	42
3.1 Load-indentation response.....	42
3.2 Indentation under low-velocity impact.....	46
3.3 Residual indentation	46
3.4 Validation.....	48
3.5 References.....	50
4 Analytical estimation of CAI strength of a sandwich with BVID.....	52
4.1 Analytical estimation of CAI strength of a sandwich with BVID.....	52
4.2 References.....	57
5 Guidelines for experimental investigations	58
6 Conclusions.....	63

Table of figures

Figure 1.1. Schematic structure of development of numerical model of sandwich panel.....	7
Figure 1.2. Schematic structure of sandwich panel.....	8
Figure 1.3. Expected fine mesh detailed finite element model of sandwich panel; a) disorderly orientated elements, b) aligned orientation of elements.....	8
Figure 1.4. Detailed shell only model.....	10
Figure 1.5. Simple shell with layup model.....	10
Figure 1.6. Solid and shell model.....	11
Figure 1.7. Solid only model.....	12
Figure 1.8. Advanced solid and shell model.....	12
Figure 1.9. Representing response of indentation simulation by surface-to-surface contact elements.....	13
Figure 1.10. Experimental adhesive material characterization.....	15
Figure 1.11. Flatwise compression of stabilized honeycomb structure (Full model).	17
Figure 1.12. Flatwise compression of stabilized honeycomb structure (3.2 mm cell).	18
Figure 1.13. Flatwise compression of stabilized honeycomb structure (6.4 mm cell).	18
Figure 1.14. Flatwise compression stiffness of stabilized honeycomb structure (6.4 mm cell).	19
Figure 1.15. Indentation ESA_035_1.....	20
Figure 1.16. Indentation ESA_027_1.....	20
Figure 1.17. Indentation ESA_027_5.....	21
Figure 1.18. Indentation ESA_039_3.....	21
Figure 1.19. Simulation of failure of UD specimen in tension.....	22
Figure 1.20. Simulation of failure of UD specimen in compression.....	22
Figure 1.21. Simulation of different degree of degradation for ESA_050_1.....	23
Figure 1.22. Indentation representation for different mesh density.....	25
Figure 1.23. Mesh sensitivity analyses.....	27
Figure 2.1. Indentation of ESA_027_5.....	28
Figure 2.2. Composite fibre failure mode according to Max stress criteria.....	29
Figure 2.3. Composite fibre failure US scan before and after impact.....	29
Figure 2.4. Residual indentation after impact.....	30
Figure 2.5. Comparison of full and reduced model stiffness for ESA_040 series..	31
Figure 2.6. Experimental curves vs. FEM_CAI (Full model) and FEM_CAI_R (Reduced model).	31
Figure 2.7. Numerical prediction (reduced model) vs. Experimental load carrying capacity ESA_040 series.....	32
Figure 2.8. Numerical prediction (reduced model) vs. Experimental test curves ESA_042 series.....	32
Figure 2.9. Numerical prediction (reduced model) vs. Experimental load carrying capacity ESA_042 series.....	33
Figure 2.10. Numerical prediction (reduced model) vs. Experimental test curves ESA_044 series.....	33
Figure 2.11. Numerical prediction (reduced model) vs. Experimental load carrying capacity ESA_044 series.....	34

Figure 2.12. Numerical prediction (reduced model) vs. Experimental test curves ESA_037 series.	35
Figure 2.13. Numerical prediction (reduced model) vs. Experimental load carrying capacity ESA_037 series.....	35
Figure 2.14. Numerical prediction (reduced model) vs. Experimental test curves ESA_035 series.	36
Figure 2.15. Numerical prediction (reduced model) vs. Experimental load carrying capacity ESA_035 series.....	36
Figure 2.16. Composite fibre failure mode according to Max stress criteria, reduced model vs. full model, ESA_027_5.	37
Figure 2.17. Numerical panel failure vs. experimental ESA_027_5.....	38
Figure 2.18. 2-ply panels with different HC density and thickness.	39
Figure 2.19. 3-ply panels with different HC density and thickness.	40
Figure 2.20. 4-ply panels with different HC density and thickness.....	41
Figure 3.1 Schematic of indentation geometry.....	43
Figure 3.2 Schematic of indentation profiles at the end of active loading (1) and upon unloading (2).....	46
Figure 3.3 Experimentally determined (“After damage”) and predicted (Analytical”) dent cross-section geometries for sandwich coupons with [0/90] facesheet lay-up upon quasi-static indentation (a) and [-60/60/0] facesheet upon low-velocity impact (b).	49
Figure 3.4. Maximum indentation depth, residual dent depth (a) and dent diameter (b) for sandwich coupons with [0/90] facesheet lay-up in quasi-static indentation as functions of maximum indentation load.	50
Figure 3.5 Residual dent depth (a) and dent diameter (b) for sandwich coupons with [0/60/-60/0] facesheet lay-up upon low-velocity impact as functions of impact energy.	50
Figure 4.1 Schematic of a side view of a sandwich facesheet (solid line) with a dent modeled as a sinusoidal geometrical imperfection (dotted line) with amplitude w_0 and half-wavelength l	53
Figure 4.2 Experimental CAI strength of sandwich coupons having [0/60/-60/0] facesheet and 20 mm thick 6.4-mm-cell core as a function of the prediction by Eq. (1).	54
Figure 4.3. Experimental CAI strength of sandwich coupons having [0/60/-60/0], [60/-60/0], or [90/0] facesheets and 30 mm thick 6.4-mm-cell core as a function of the prediction by Eq. (1).	55
Figure 4.4. Experimental CAI strength of sandwich coupons having [0/60/-60/0] and [60/-60/0], facesheets and 20 mm thick 3.2-mm-cell core as a function of the prediction by Eq. (1).	55
Figure 4.5 Experimental CAI strength of sandwich coupons having [0/60/-60/0], [60/-60/0], or [90/0] facesheets and 30 mm thick 3.2-mm-cell core as a function of the prediction by Eq. (1).	56
Figure 5.1 Gas bubbles in adhesive resin coupon specimens.....	59
Figure 5.2 US scan of thickness distribution along the skin panel.	60
Figure 5.3 Panel cut to individual specimens.....	60
Figure 5.4 Strain distribution measurement along the panel width.....	61
Figure 5.5 Measured strain distribution along the panel width.....	61
Figure 5.6 Specimen ends with non-planar edges.....	62

Introduction

A current report summarise efforts and lessons learned in order to develop and validate the numerical simulation model by commercial finite element code ANSYS [1]. Each chapter analyses and present findings for a specific change on numerical/analytical or experimental procedures; nevertheless all chapters are physically validated in order to formulate valid conclusions.

The numerical modelling includes a finite element type, mesh as well as sensitivity analysis of selected material properties. For element, type studies both shell only and shell/solid element types were investigated. In order to find best trade-off between model prediction reliability and CPU cost a mesh sensitivity was studied for both element type models. A combination of shell and solid model have been identified as the most appropriate for both CPU cost and robustness of the solution are in trade off with physical experiment. It should be noted, that initially actual honeycomb model has been replaced with equivalent – volume representative elements, which accounts for material nonlinearities, and linked with plasticity behaviour of aluminium foil honeycomb. Nevertheless, a full model analysis was build and validation among other numerical and experimental approaches performed.

Initially while only few specimens were build, the verification phase included numerical modal analysis only. This early verification step allowed updating analysis strategy in early stage of development. From numerical simulation point of view, linear analyses are very robust and fast therefore simple in verification of assumptions included in numerical analysis.

It has been followed by more sophisticated finite element model consisted of shell/solid modelled honeycomb structure, covered by two CFRP shell face sheets. Shell element model, incorporates tied face sheet to honeycomb connection by sheared nodes, thus eliminating possible skin delamination damage propagation. Due to presence of buckling of honeycomb cell walls, minimum element size was determined to be set as $\frac{1}{2}$ of the cell size (1.5 mm), to allow the walls to form buckles. Adhesive layer added to the skin lay-up, as additional layer with corresponding material properties and material plasticity model. Honeycomb structure model has been set to incorporate multilinear isotropic hardening plasticity material model based on experimental characterization. Moreover, composite progressive damage model was integrated, based on characterization of material properties of UD composite. Composite progressive damage model realized through max stress criteria with material stiffness degradation. Interaction between indenter and panel surface was modelled as surface-to-surface contact.

Numerical and analytical approach for indentation of sandwich panel have been validated with physical experiments and full range of results have been uploaded on projects web page: http://bnm4eks.rtu.lv/tools_en.html. Several further steps have been identified and will be incorporated in final deliverable focusing on numerical analysis best design practice.

Finally, guidelines for experimental testing are formulated including the tips for specimen preparation/assembly and testing. Those guidelines share best practice derived from extensive experimental work defining specimen preparation procedure, fixture potting and test set-up.

1 General consideration in development of numerical model

1.1 Numerical model development strategies for finite element method

Current report focusing on sandwich honeycomb structure numerical model strategies, advantages and disadvantages applicable for commercial finite element method (FEM) code ANSYS in particular, but can be applicable to other codes which employs iterative quasi-static solvers (Newton-Raphson iterative solver). Two finite element model concepts were considered during preliminary study. In general, model consist of two relatively thin skins, aluminium honeycomb sandwich core and adhesive layers bonding them together. In numerical model all, geometrical, material and element assumptions should be considered as parametrical input variables, according to a variety of components used (honeycomb size, thickness, face sheet lay-up, indenter diameter and indentation depth, etc.). This approach allows user to modify ply stacking sequence and thickness of all layers, as well as panel length, width and height. Material models includes mechanical properties for composite skins including failure criteria and progressive damage propagation mechanism, plasticity of aluminium honeycomb core, as well as, adhesive layer plasticity and skin debonding mechanism.

In general development of the numerical model of the sandwich panel used for prediction of load carrying capacity of edgewise loaded specimens consider multiple cross references with preliminary studies of material and structural experimental investigation, Fig. 1.1. Starting with coupon test data on material characterization for different panel components (skin composite, adhesives, honeycomb material, etc.) with accompanied numerical validation of those properties. Following steps were panel level validation of the indentation process and finally edgewise compression test (CAI) validation with completely developed model.

Numerical simulations of sandwich structures

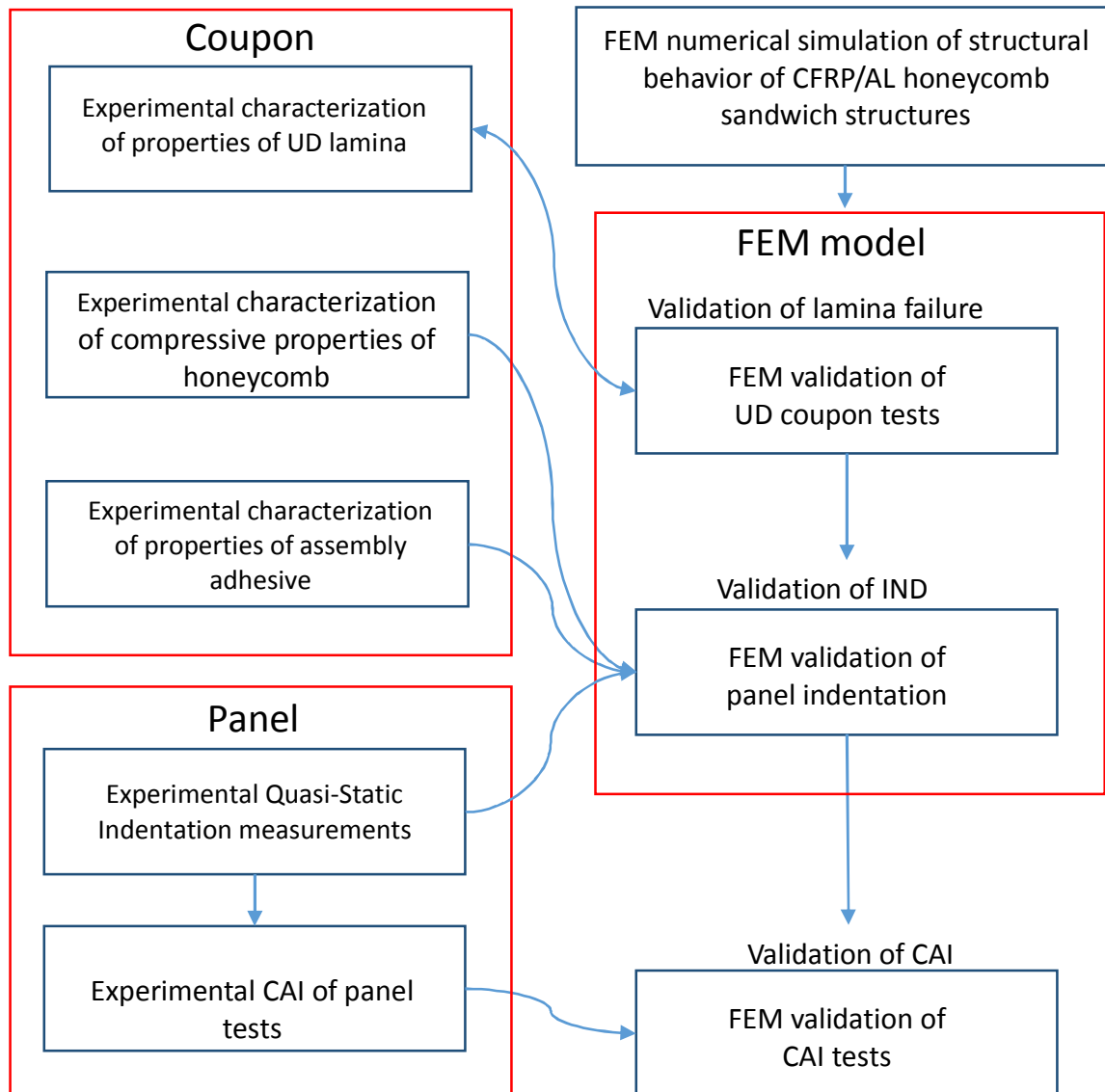


Figure 1.1. Schematic structure of development of numerical model of sandwich panel.

Two major approaches for honeycomb sandwich structure finite element model were considered for present study needs. Both models includes plasticity of honeycomb core (residual deformation caused by external impact loading), possible composite damage with damage propagation mechanism. Availability of experimentally obtained data on honeycomb structure mechanical properties, such as transverse stiffness, longitudinal stiffness, plasticity propagation, adhesive properties etc., will narrowing selection of appropriate finite element model type and applicability.

So called, (Full model), which represents actual honeycomb sandwich structure composed by shell elements and simplified (Reduced model), where aluminium core was substituted by solid volume elements. All structural parts are

represented by shell elements, except for Reduced model, Fig. 1.2. Both skins modelled as layered composite shells, incorporating additional adhesive layer. Honeycomb structure, composed as 3D shell structure, or 3D solid volume in Reduced model.

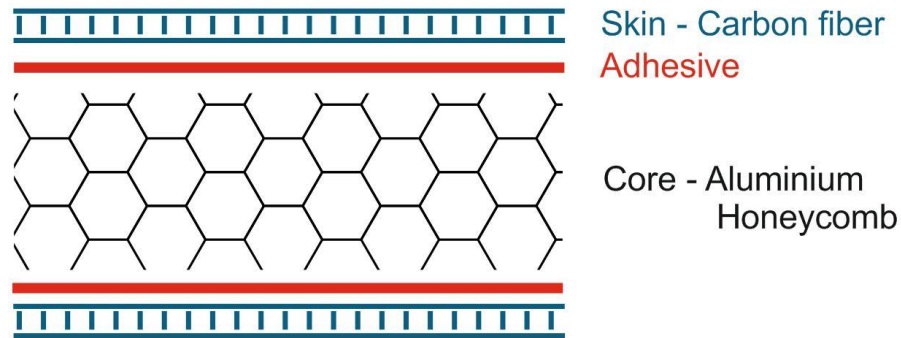


Figure 1.2. Schematic structure of sandwich panel.

For selection of types of numerical model for honeycomb sandwich structure, a particular attention should be paid to finite element mesh size (total model DOF size) and required computation time. As long as parametrical model involves a number of related parameters, to avoid model complexity a uniform fine mesh will be expected to be the most accurate, nevertheless considering local defects on full scale panels are extremely time-costly, balance between mesh density, available solver hardware and acceptable representation of results should be found. An example of expected FEM numerical model shown in Fig. 1.3. Initial model should be double checked for numerous sources of errors including: local orientation of elements (Fig. 1.3 a/b) which assures correct assumptions of stacking sequence and material properties, correct thickness of shells and nodal plane offsets, contact surface normal orientation, etc.).

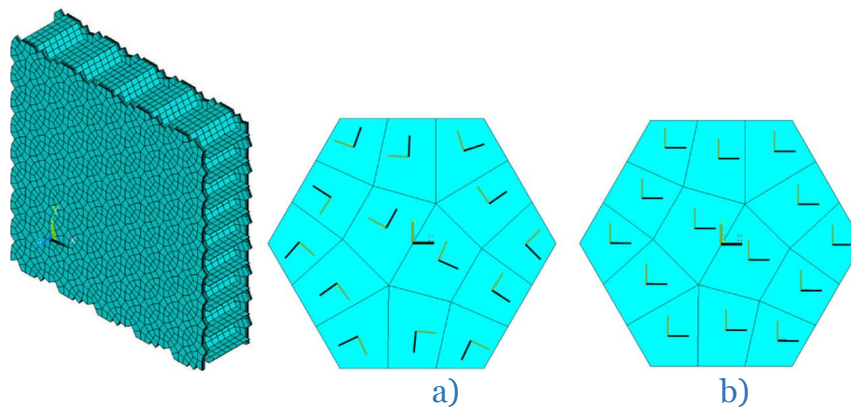


Figure 1.3. Expected fine mesh detailed finite element model of sandwich panel; a) disorderly orientated elements, b) aligned orientation of elements.

Initial finite element mesh size correlation should be revisited during verification steps and validation stage. Such practice would guarantee efficiency and robustness of developed model. In case of real honeycomb structure representation, it should be noted that minimum required number of element along honeycomb hexagon side will be 2, thus ensuring that honeycomb wall will be capable to buckle

under indentation forces or forces introduced by inward skin penetration during CAI stage. One element per side model was not accepted, due to lack of buckling ability of the honeycomb structure wall, but can be applicable together with element mesh refinement in the region of indentation and dimple propagation during CAI stage. In the present study, models with refined mesh in the indentation region were used only for comparison reasons, due to complicated (non-controllable) mesh refinement, which often involved meshing errors and unreasonable increase in DOF size. On the other hand, larger element division can lead to more accurate buckling representation, since buckled wall will be smoother, which helps for easier convergence of the solution, but at the same time, it will lead to unnecessary higher DOF number and increase of computation time. In case of reduced model initial element size should be enough to represent skin dimples and buckling with at least five elements per dimple side.

1.2 Element type assumptions

Whether shell or solid element type assumption should be considered for numerical analyses. Nevertheless, both alternative approaches offer a lot of variety how numerical model should be finally composed. If sandwich structure is entirely built from shells including topology of honeycomb structure, the model consists of extremely large number of elements, especially for honeycomb core with small cell size (3.2 mm), (Figure 1.4). On the contrary single shell model allows on simple geometry to integrate several layers including honeycomb core and adhesive layer (Figure 1.5). Having such an approach restricts introduction and assessment of residual indentation due to single nodal plane, while for other applications with multi ply interaction, this approach was considered as most efficient. To simulate indentation introduced residual dimple and to reduce complexity of model a solid volume element representation of the honeycomb structure combined with shell element skin plies, Fig. 1.6, are more ingenious approach compared to fully solid element model, Fig. 1.7. As in particularly of thin walled structures solids are not suited to represent stacking sequence of thin layered skin, due to improporionally high element size aspect ratio of thickness to element dimensions, otherwise taking into account small layer thickness, element dimensions will lead to unnormous number of elements. The most advanced and currently widely used approach could be to combine both shell element structure in area of indentation, surrounded by solid element core, Fig. 1.8. The greatest disadvantage of this approach was complexity of the interaction of model parts composed by different element types, due to parametrical input of dimensions and part connections. Taking all considerations into account two major approaches of development of numerical model was considered in current study: Full shell model and Reduced shell/solid model.

1.2.1 Shell element SHELL 281

The most advanced shell element SHELL 281, at the present time, of finite element code ANSYS [1] was designed for analyses of thin to moderately-thick shell structures. SHELL 281 is eight node element with six degrees of freedom at each

node: translations in the x, y, and z axes, and rotations about the x, y, and z-axes. SHELL 281 is well-suited for full range of applications: linear, large rotation, large strain nonlinear analyses. Element formulation taking into account for change in shell thickness during nonlinear large deformation analyses. As well as, non-linear material properties, composite damage, plasticity, etc. SHELL 281 can be used for layered applications for modelling composite shells or sandwich construction. The accuracy in modelling composite shells was governed by the first-order shear-deformation theory (usually referred to as Mindlin-Reissner shell theory).

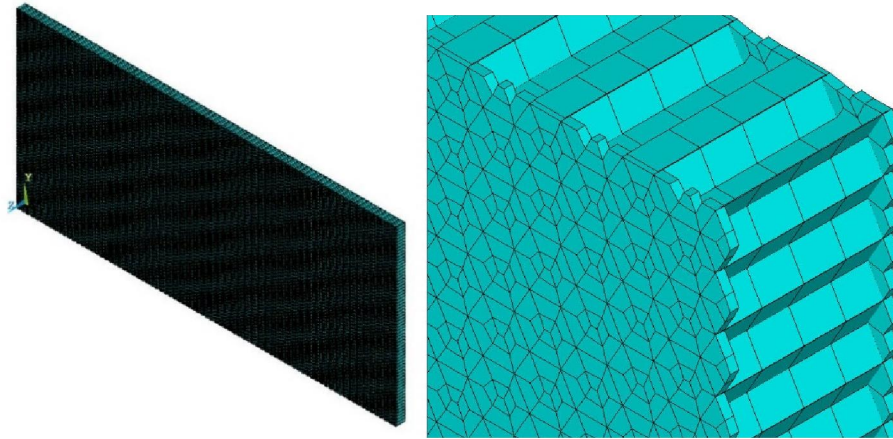


Figure 1.4. Detailed shell only model.

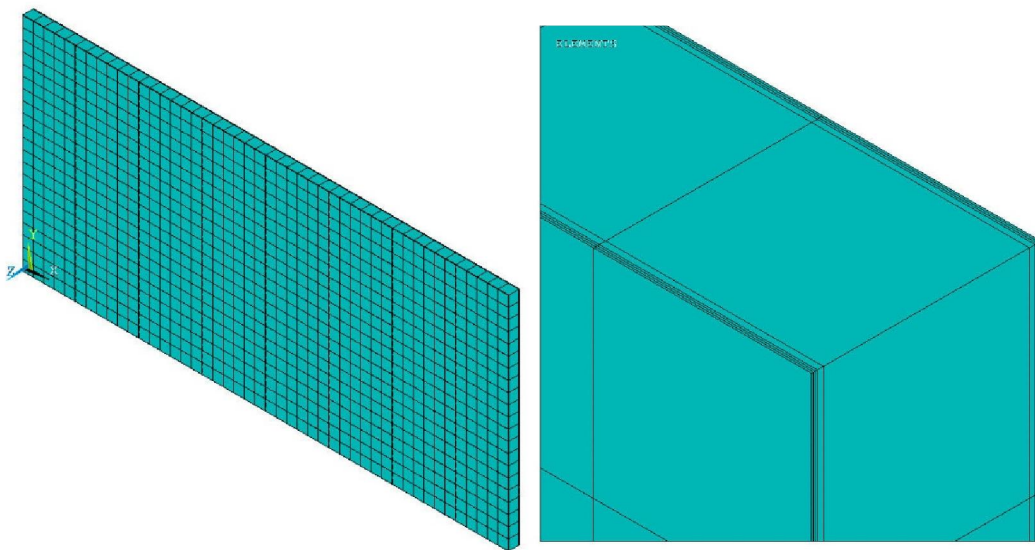


Figure 1.5. Simple shell with layup model.

1.2.2 Solid element SOLID186

SOLID187 is a higher order 3-D 10-node tetrahedron solid element that exhibits quadratic displacement behaviour. 20-node brick elements can be used as well for core representation, while should be avoided for indenter semispheric volume due to meshing errors, where pyramid shaped 10-node elements are preferable. The element is defined by 10 nodes, having three degrees of freedom per node: translations in the nodal x, y, and z directions. The element supports plasticity,

hyperelasticity, creep, stress stiffening, large deflection, and large strain capabilities. It should be noted that compared with simple shell with stacking sequence the degrees of freedom per model are by magnitude lower than shell only model (Figure 1.4). Nevertheless, refinement of solid element mesh in area of indent are quite complex and should be advanced with caution, especially in combination with parametric modelling.

Substitution of the real honeycomb structure modelled by shell elements with the volume, modeled by structural solid elements (SOLID187), Fig. 1.6, with considered Hill plasticity behaviour of honeycomb core elements. The fact that honeycomb structure has considerably higher stiffness and plasticity properties for transverse (through thickness) axis in comparison to in-plane properties, should be realized through use of Hill plasticity rule. Reduced finite element model also considered as model, which incorporated possible face sheet delamination from the core, by incorporating cohesive zone material de-bonding contact between face sheets and core volume. As well as, incorporating plasticity model for assembling adhesive layer used for better indentation representation, due to available adhesive material data. Disadvantage of the full shell models was that debonding was not applicable due to skin honeycomb element connection through shared nodes. This feature theoretically can be included, with more sophisticated surface to node contact representation in full model.

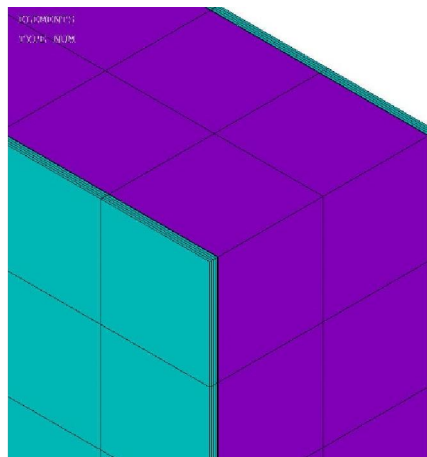


Figure 1.6. Solid and shell model

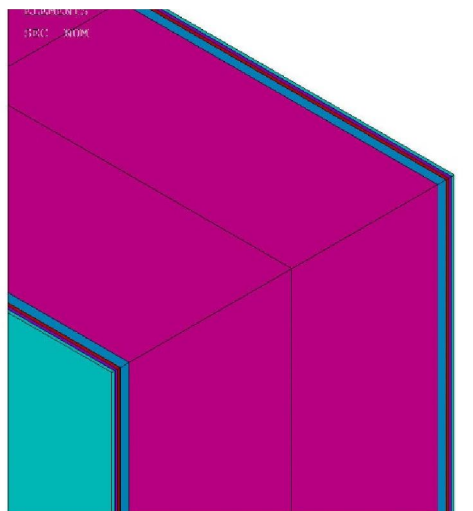


Figure 1.7. Solid only model

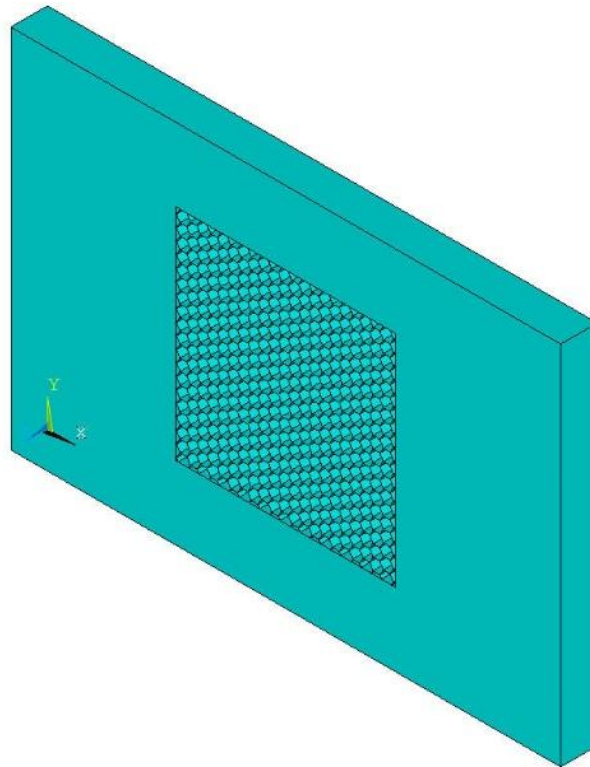


Figure 1.8. Advanced solid and shell model

1.2.1 Contact interface elements

Indentation interaction between the impactor, modelled as rigid 3D volume (SOLID187) semi-sphere and the panel skin (SHELL281) was modelled by the use of surface-to-surface contact elements. For all models involving contact interaction between indenter rigid body and panel surface, contact behaviour was selected as deformable surfaces-to-surface contact, employing surface contact elements TARGE 170 and CONTA174 in ANSYS commercial software. Contact element mesh density was the same as underlying structural elements, maintaining correct normal orientation. Contact element normal orientation should be checked to contact algorithm worked. Contact separation should be allowed. Since indenter was modeled with slight offset from the panel surface to avoid problems of automatic node selection used for different manipulations, an initial contact closure algorithm should be turned on, to close the initial gap and avoid rigid body motion at the start of analyses run. Indenter body material assumed to be elastic, with steel material properties and friction coefficient of 0.3.

For both models, indenter motion should be controlled by displacement, to introduce the same amount of deformation for both models. It is possible to introduce indentation with load application, but it can introduce highly incorrect indentation depth due to possible incorrect representation of core material properties for different models.

While Full model incorporates direct connection of hexagonal areas of the skin to the honeycomb structure edges, by shared nodes, Reduced model incorporates skin

shell element connection to the solid volume core elements by the bonded contact interface elements with Cohesive Zone Material (CZM) model. CZM incorporates possibility of skin debonding based on Mode I debonding (in this particular task), which defines a mode of separation of the interface surfaces where the separation normal to the interface dominates the slip tangent to the interface. The normal contact stress (tension) and contact gap behavior is plotted in Fig. 1.9. It shows linear elastic loading (OA) followed by linear softening (AC). The maximum normal contact stress is achieved at point A . Debonding begins at point A and is completed at point C when the normal contact stress reaches zero value; any further separation occurs without any normal contact stress. The area under the curve OAC is the energy released due to debonding and is called the critical fracture energy. The slope of the line OA determines the contact gap at the maximum normal contact stress and, hence, characterizes how the normal contact stress decreases with the contact gap, i.e., whether the fracture is brittle or ductile. After debonding has been initiated it is assumed to be cumulative and any unloading and subsequent reloading occurs in a linear elastic manner along line OB at a more gradual slope [1]. Contact separation based on bilinear material behavior was implemented in this study, since the data of skin separation can be obtained from peel drum test.

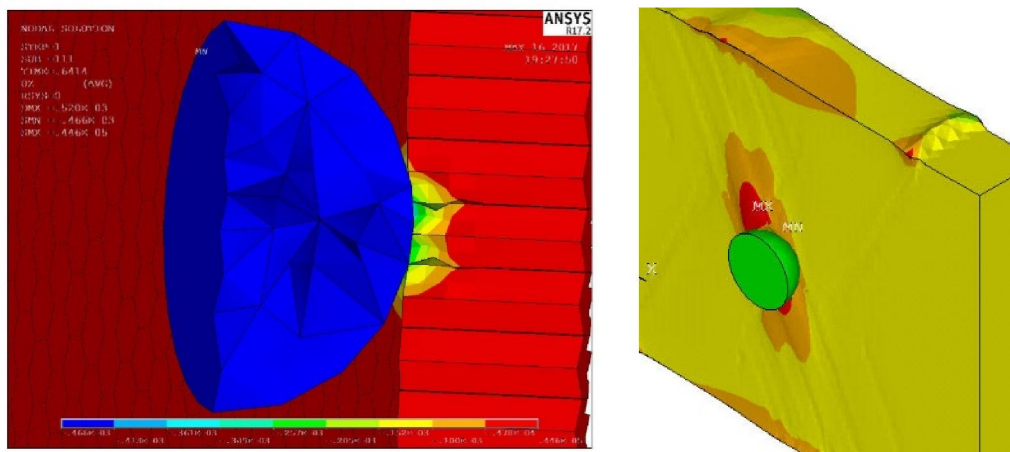
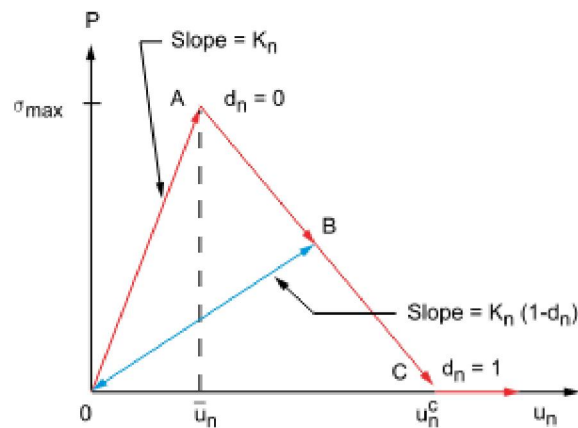


Figure 1.9. Representing response of indentation simulation by surface-to-surface contact elements.

1.3 Material models

Experimental characterization of mechanical properties of all materials incorporated in sandwich panel model are obtained experimentally. This include sandwich panel skin, carbon fibre reinforced plastic (CFRP) orthotropic material stiffness's and limiting stress/strain values. Adhesive layer experimental tests were carried out with the purpose to include the plasticity model for bonding layer in numerical model. A simple coupon tests on tension and compression was carried out to characterize mechanical properties and plastic behaviour of the adhesive material used for assembling CFRP face sheet to honeycomb core. Unipreg CFRP material properties extracted experimentally are detailed outlined in coupon testing deliverable and average values integrated in FEM are summarised in Table 1.1.

Due to significant adhesive layer thickness, comparable or even exceeded face sheet thickness it was decided to include adhesive layer plasticity into finite element model as bi-linear isotropic hardening material model with experimentally obtained E-modulus (1.97 GPa), yield stress (49 MPa) and tangential modulus (0.01 GPa), Figure 1.10. This assumption is robust enough in case of panel damage propagation due to delamination. Possible damage propagation due delamination/debonding was taken into account by cohesive zone material (CZM) modelling technique, which realized by the debonding contact algorithm employing maximum debonding normal stress (1.5 MPa) and crack propagation energy (575 J/m²), obtained from experimental drum peel tests in combination with bi-linear material model. Cohesive zone material (CZM) model was implemented in shell-solid (Reduced) model by the use of contact element interface between honeycomb core and face sheet.

Table 1.1. Unipreg CFRP material properties

Property		Mean values								
		Unipreg 100 g/m ²			Unipreg 200 g/m ²			Unipreg 200 g/m ² (high stiffness)		
E ^t , GPa	0°	122.69	115.91	75.52	124.09	122.55	73.33	164.62	164.11	108.37
	90°	8.39	7.79	8.91	6.43	6.63	7.86	-		
E ^c , GPa	0°	103.91	102.77		117.60	121.1		-		
	90°	7.70	7.00		7.60	7.84		-		
E ^f , GPa		112.83			106.03			-		
G ₁₂ ^{chord} , GPa		6.07	5.78		4.66	4.05		-		
G ₁₂ , GPa		3.00			3.71			-		
G ₁₃ , GPa		2.45			2.77			-		
μ	0°	0.33			0.37			0.38		
R ^t , MPa	0°	1466			1539			2037		
	90°	46			41			-		
R ^c , MPa	0°	481			752			-		
	90°	138			141			-		
τ ₁₂ ^m , MPa		53			50			-		
R ^f , MPa		1427			1217			-		
u ₁₂ , MPa		207			233			-		
u ₁₃ , MPa		654			2009			-		

Due to two step analysis procedure – indentation first, followed by edgewise compression (CAI) there were no failure criteria implemented for adhesive material model, in order to avoid excessive stiffness softening in region of indentation caused by failure of material at the tension side of the face sheet, which later was loaded in axial compression. In other words, if failure of adhesive was detected due to indentation of impactor in the face skin. Corresponding finite element stiffness was decreased by 99%. Nevertheless, if and only in case of following pure compressive loading the cracked adhesive layer will sustain (lock down) the compression despite the inherited crack. Thus though eliminated stiffness of delamination affected elements and exclusion of them from further model analysis the local stiffness at impact region will be decreased.

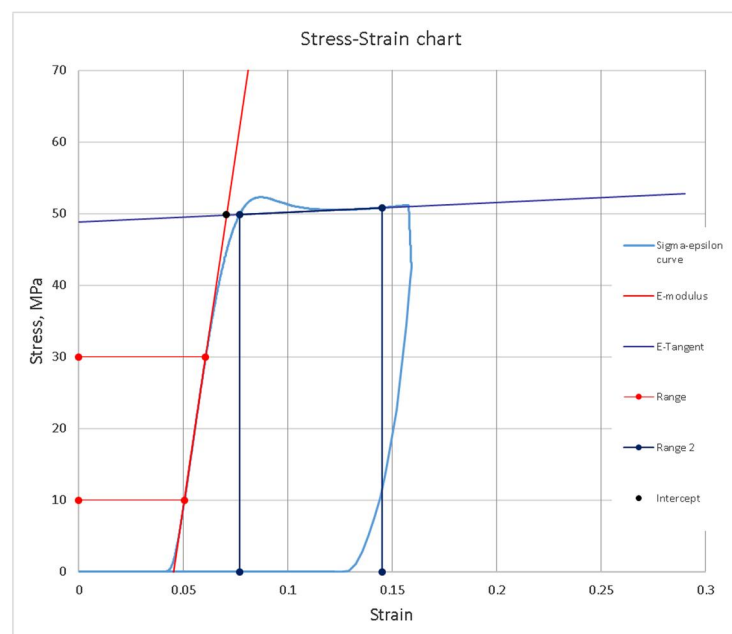


Figure 1.10. Experimental adhesive material characterization.

The characterization of material properties of AL honeycomb core was performed experimentally to determine structural properties used for implementation in reduced finite element model as Hill plasticity rule in combination with bi-linear isotropic hardening plasticity model. Due to significant difference in stiffness of the honeycomb structure for in-plane and out-of-plane axis, Hill plasticity rule with ratio of 0.05 for in-plane axis and 1.0 for out-of-plane axis was introduced in finite element model. This was considered in combination with bi-linear isotropic hardening material model. Out-of-plane compressive properties was experimentally characterized by flatwise compression of stabilized honeycomb structure, Figure 1.14. Stress values of honeycomb buckling (σ_B) and crushing stress (σ_{CR}) in combination with accompanying (E_{core}) modulus and (E_{tan}) tangent modulus, was used in finite element model for honeycomb structure material representation based on experimentally measured values. Full model incorporate aluminium material properties accompanied by available strength and plasticity data for AW 6082 T6 alloy.

Another alternative pressure-dependent extension of Hill's quadratic yield criterion which has a form similar to the Bresler Pister yield criterion is the Deshpande, Fleck

and Ashby (DFA) yield criterion for honeycomb structures (used for sandwich composite construction) which can be implemented in finite element code by user.

Table 1.2. Material properties of AW6082 T6 alloy.

	Strain	Stress	E
Point	m/m	MPa	GPa
1	0	0	
2	0.003	210	70.00
3	0.004	254	44.00
4	0.005	268	14.00
5	0.0075	283	6.00
6	0.01	293	4.00
7	0.02	308	1.50
8	0.035	328	1.33
9	0.05	334	0.40

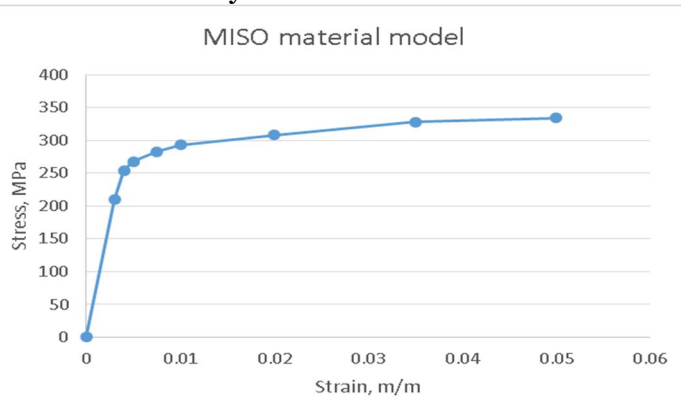


Table 1.3. Honeycomb flatwise compression material properties.

	HC core	
Material	3.2 mm	6.4 mm
properties	MPa	MPa
E_{core}	573	202
E_{tan}	1	1
σ_b	2.10	0.82
σ_{CR}	1.00	0.24

Numerical validation of the flatwise compression of the honeycomb structure showed considerable difference in flatwise compression stiffness between idealized (perfect) full model representation, based on buckling stiffness of the perfect geometry cell structure composed of shell elements, Fig. 1.12 and simplified volume representation (reduced model) based on experimental stiffness. Fig. 1.13 shows that material model based on experimental data used for reduced model is in good agreement in terms of stiffness and plasticity onset with corresponding experimental curve. On the other hand, the major drawback of this approach is inability to represent negative tangent branch by the finite element code material model, which clearly observed on experimental curve, caused by buckling of cell walls. Full model behaviour is more realistic in comparison to experimental curve, facilitating negative drop of stiffness caused by actual buckling of cells, but with less severity and much higher initial stiffness slope (possibly caused by some geometrical imperfections, which presents in actual honeycomb structure).

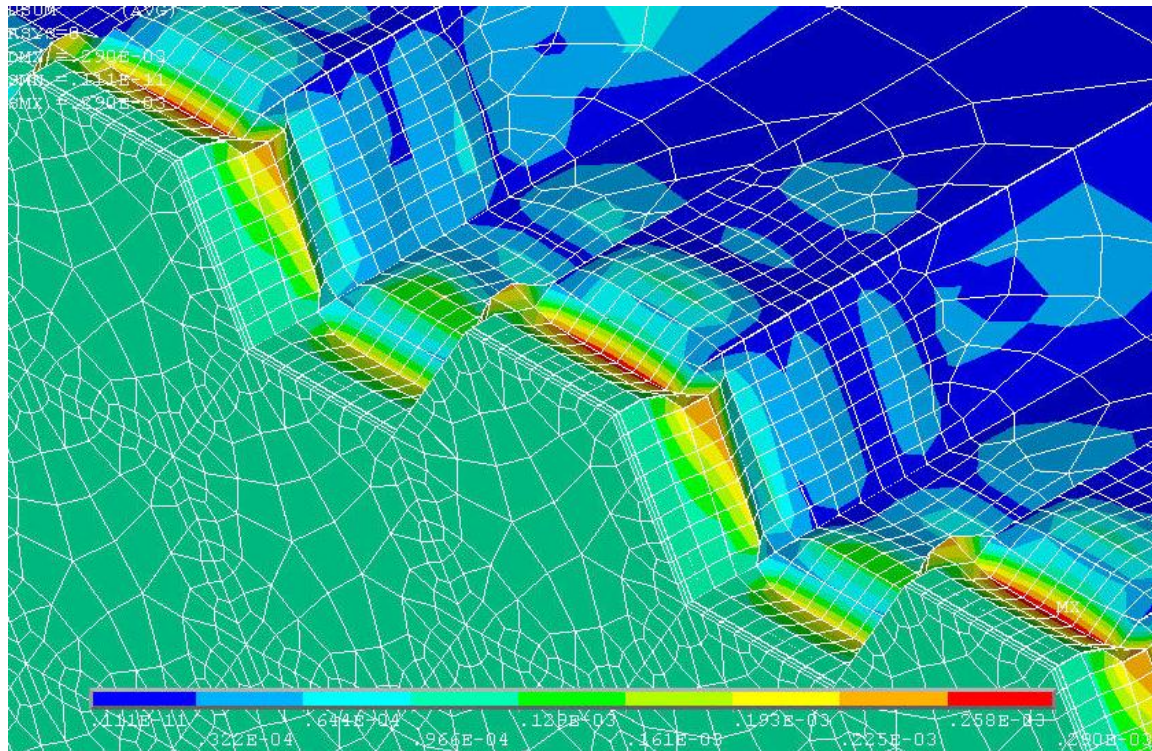


Figure 1.11. Flatwise compression of stabilized honeycomb structure (Full model).

Deeper investigations in plasticity representation and adjustment of related material properties (Poisson`s ratio) and Hill plasticity model, can lead to improved stress-strain representation for reduced finite element model. Further refinement of the finite element mesh of the full model produced even higher load carrying capacity of the honeycomb structure (performed for 6.4 mm cell honeycomb core only). Analyses of the stiffness of the both numerical models, Fig. 1.14, showed about 2 to 2.5 x higher stiffness of the full model compared to reduced model, which based on experimental data. Such increased stiffness resulted in proportionally higher indentation loads obtained with full model in comparison with reduced model. It should be noted, that stiffness and strength of the honeycomb subjected to uniform flatwise compression not dependent on honeycomb panel thickness.

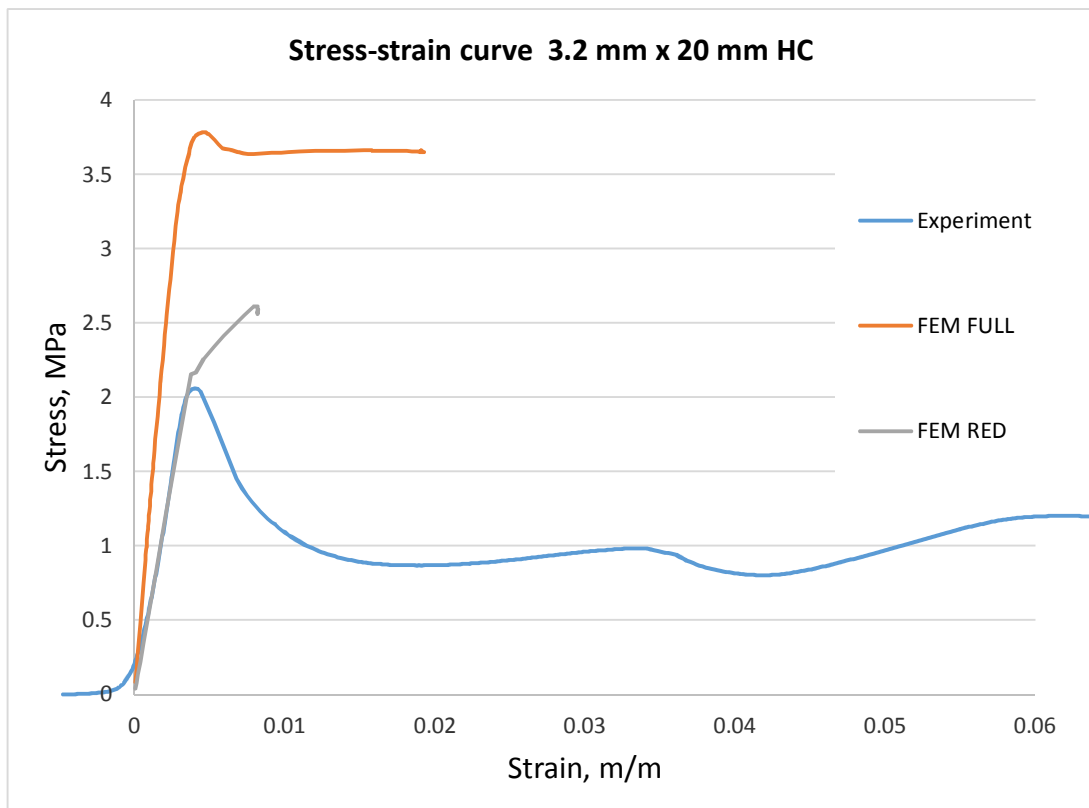


Figure 1.12. Flatwise compression of stabilized honeycomb structure (3.2 mm cell).

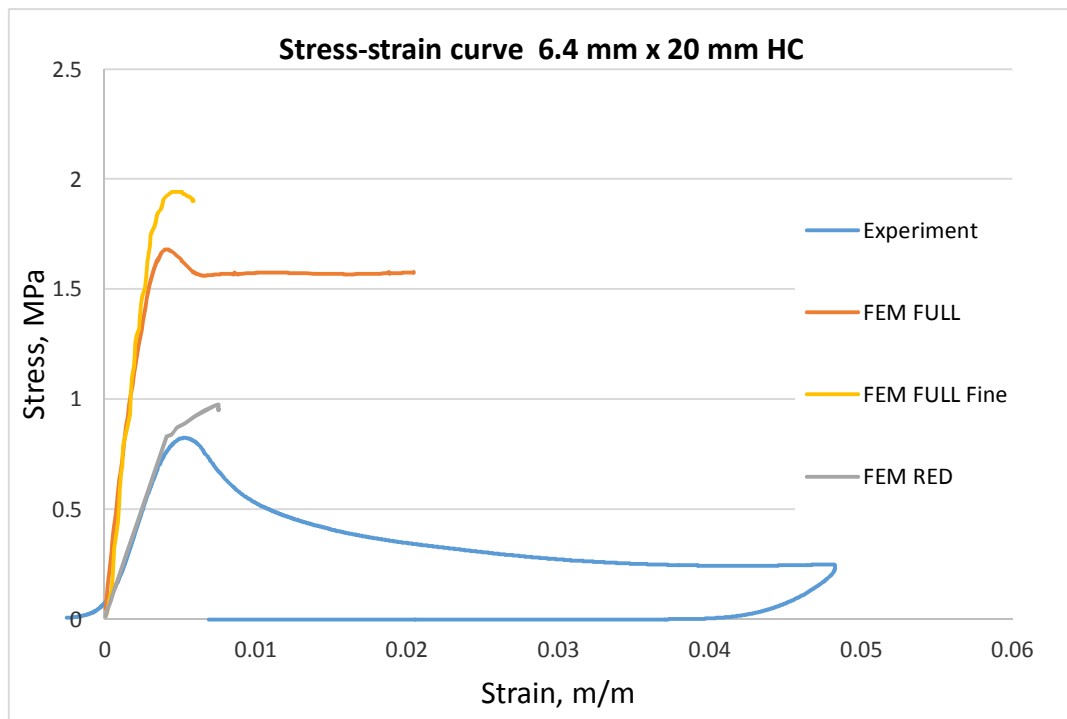


Figure 1.13. Flatwise compression of stabilized honeycomb structure (6.4 mm cell).

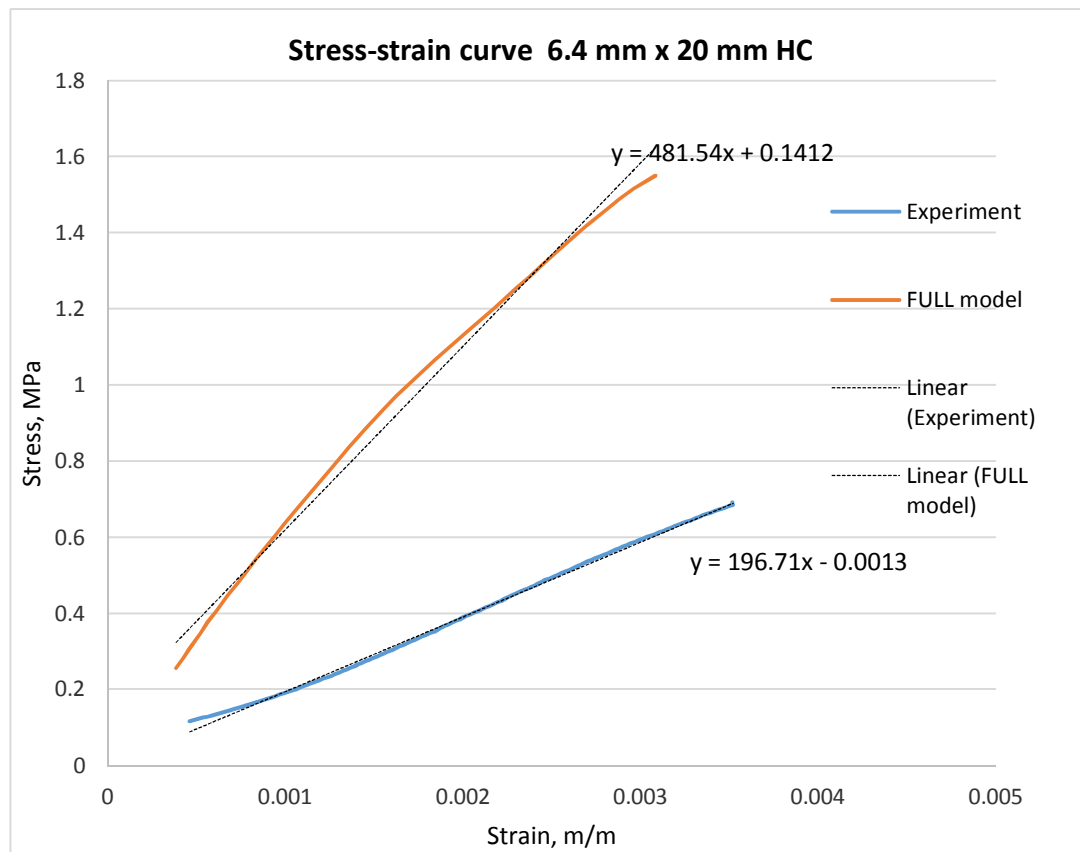


Figure 1.14. Flatwise compression stiffness of stabilized honeycomb structure (6.4 mm cell).

Validation of the plasticity models incorporated in finite element models was performed on selected panels with different lay-ups and core thickness, Fig. 1.15, Fig. 1.16, Fig. 1.17 and Fig. 1.18, by comparison of indentation force-displacement curves for both finite element models and experiment. It should be noted that despite superior stiffness of full model compared to experimental and reduced model, force – displacement curve reaches zero load during unloading at almost the same spot for different lay-up specimens, with some exceptions. In reality, this “zero load” spot indicates depth of the indentation caused by plasticity. For some unknown reasons for vast majority of specimen residual indentation depth measured by laser sensor was much less than obtained by both numerical models, even for those reached “zero spot” in close proximity. As mentioned above higher compressive stiffness of the full model resulting in higher indentation force, which can be considerably reduced with refinement of the element size in the region of indentation at least 2x (element size 0.7 – 1.0 mm). This refinement in some cases will decrease residual indentation (zero load point) at highly increased computational cost, but in most cases will deliver the same amount of residual indentation as coarse mesh model. In most cases refined full models indicated decreased indentation force showing better correlation with experimental data and reduced model. Reduced model in most cases was in good agreement with experimental data. Despite this reduced models showed much higher residual deformations (dimples), compared to full model and experiment. This can be corrected by refined investigations in plasticity model implementation for reduced model.

High stiffness of the numerical model will produce incorrect indentation depth in case of load controlled indentation, thus direct displacement controlled indenter loading is preferable, at least for quasi-static indentation.

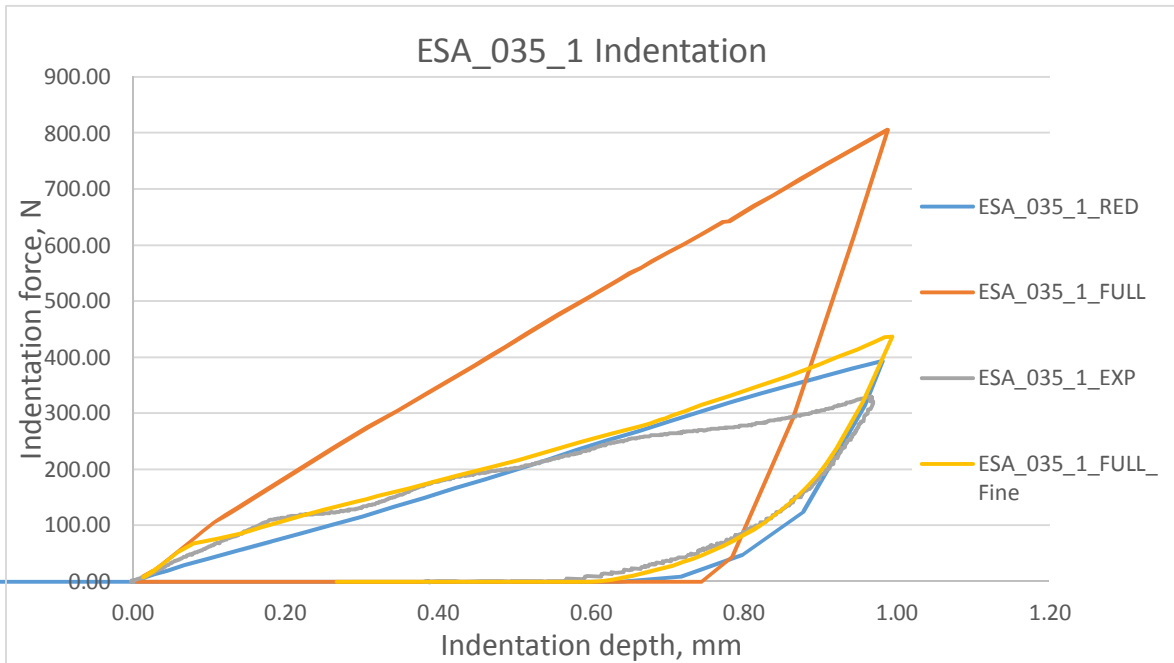


Figure 1.15. Indentation ESA_035_1.

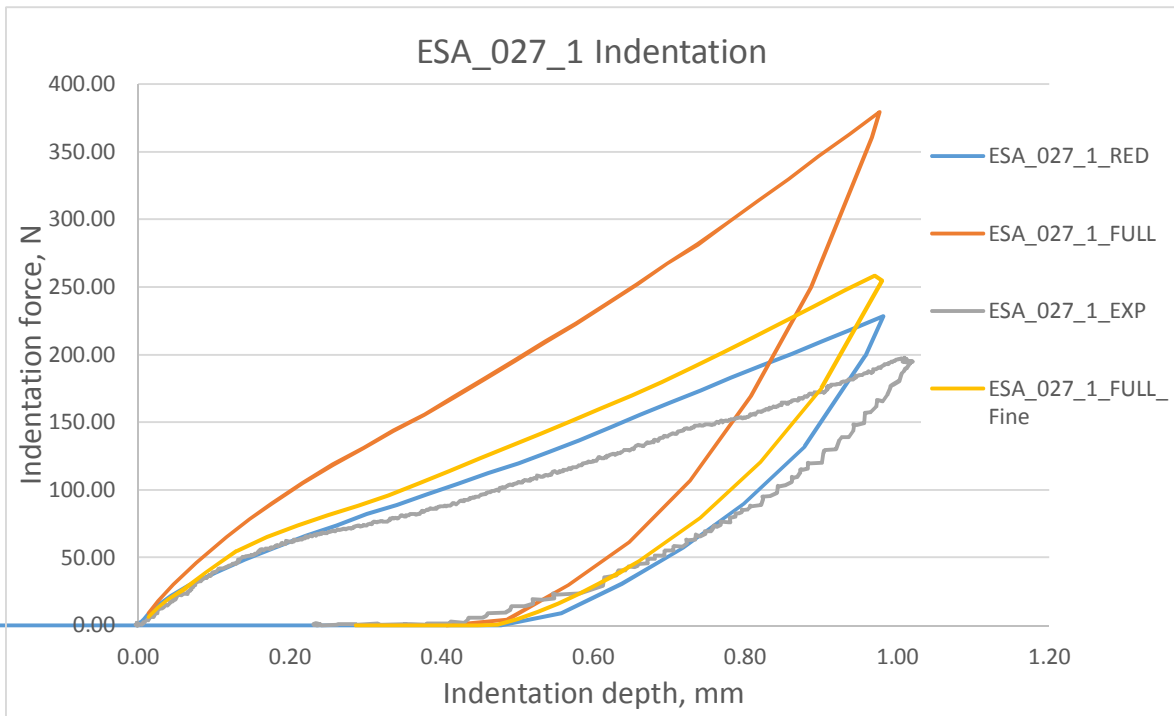


Figure 1.16. Indentation ESA_027_1.

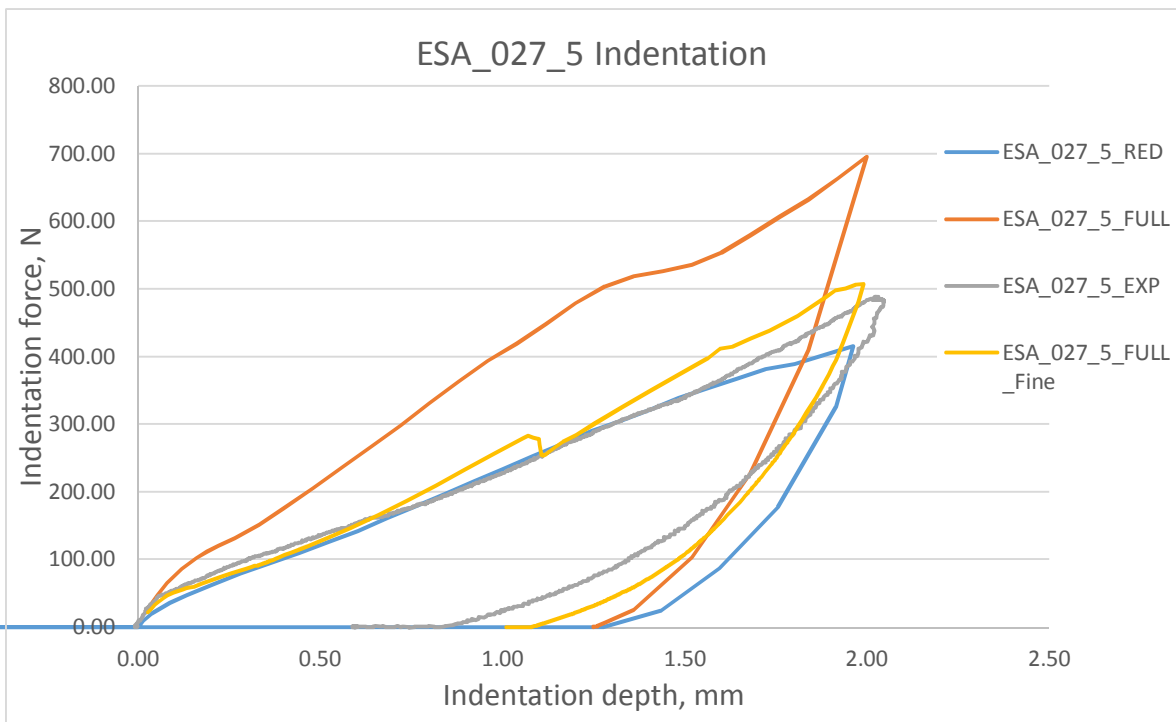


Figure 1.17. Indentation ESA_027_5.

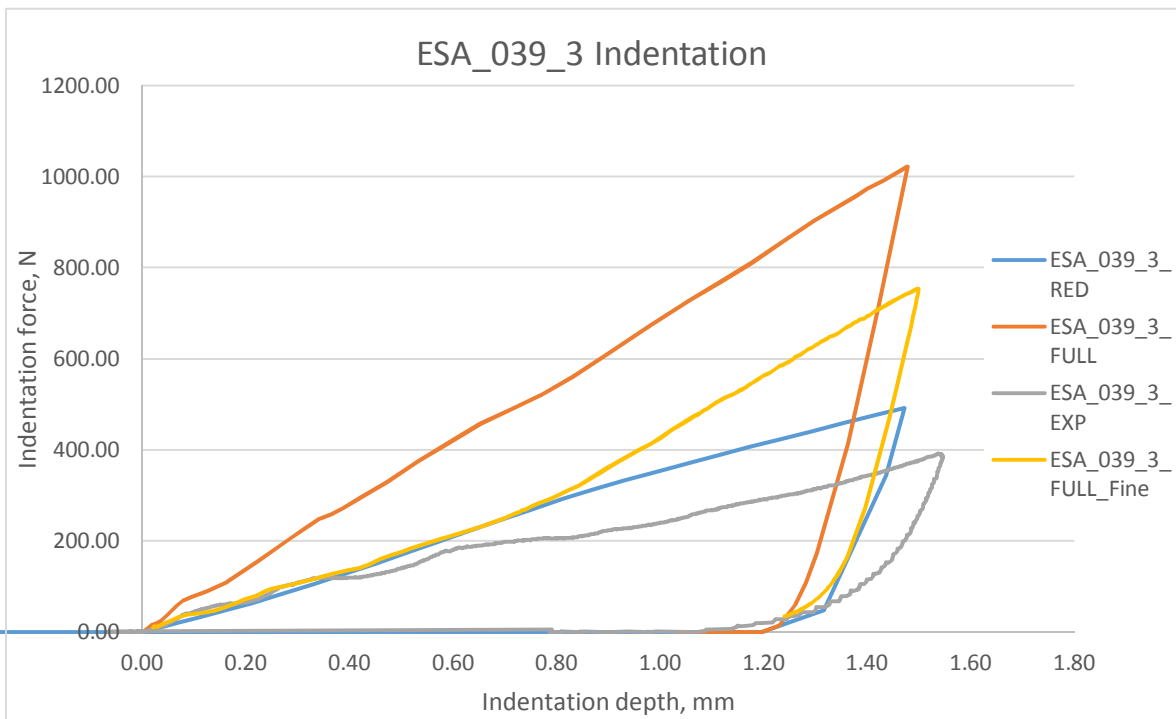


Figure 1.18. Indentation ESA_039_3.

1.4 Validation of lamina failure criteria

UD lamina properties obtained during characterization of mechanical properties of UD composite, was used as material properties and failure criteria for

both finite element models. UD coupon test simulations with FEM models to validate experimentally obtained failure criteria was carried out for tension and compression of UD specimens with actual cross-section. Comparison was rated in terms of stiffness slope and failure load. Figure 1.19 represents axial tension of UD specimen, and Figure 1.20 represents axial compression of UD specimen. Failure criteria based on Max stress initiation and material stiffness reduction damage evolution law was used for this study [1]. It is obvious that the most satisfied results were obtained for axially loaded specimens, while transversally loaded and shear ($\pm 45^\circ$) specimens, which are more sensible to damage introduced during specimen manufacturing, was less successive. For axially loaded specimens, especially for tension loaded, there was observed good correlation in terms of stiffness and breaking load, between experiment and simulation. While compression test simulation was not as successful as tension, having slightly different stiffness, but clearly the same breaking load. This indicates that in common, selected failure criteria in combination with selected damage evolution law, work as expected and can be implemented for composite part model for sandwich modelling.

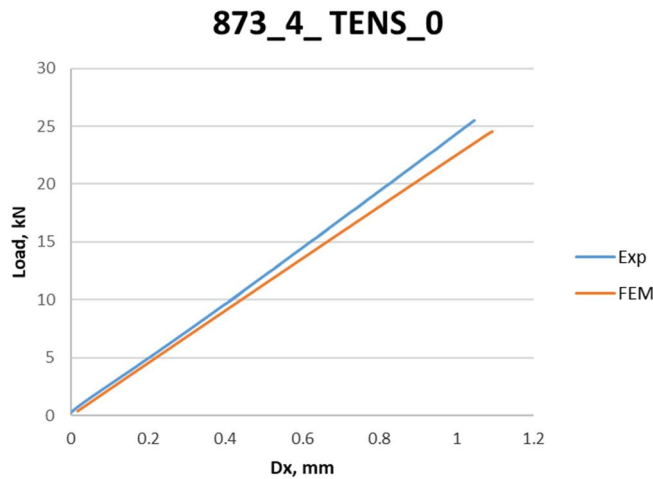


Figure 1.19. Simulation of failure of UD specimen in tension.

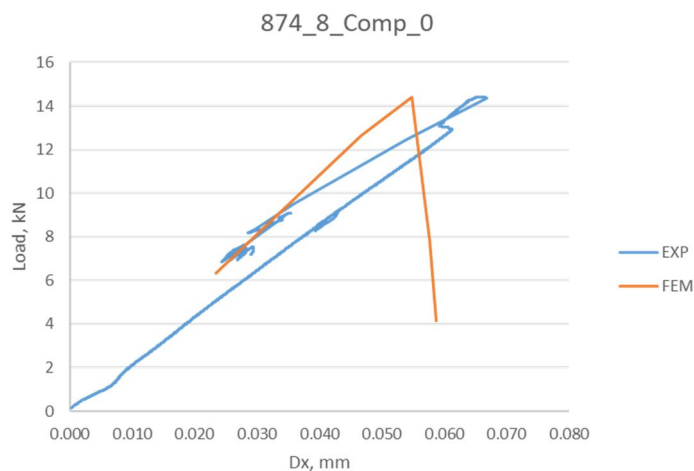


Figure 1.20. Simulation of failure of UD specimen in compression.

Comparative study on effect of progressive damage evolution mechanism, based on amount of reduction of stiffness, was carried out for one particular

specimen (ESA_050_1) in comparison to experimentally obtained load-shortening curve. Fig. 1.21, shows that despite much lower numerically obtained load carrying capacity, complete (99%) reduction of stiffness produces more realistic post-collapse behaviour, typical for majority of the experimentally tested specimens, having stable zero slope without load increase, which was not observed for lesser stiffness reduction (0.85, 0.75, etc.). On the other hand, there are some point of stiffness change (about 20 kN), common for all levels of degradation, which indicates load level at which skin penetration forces pass the honeycomb resistance forces (plasticity), leading to collapse. Theoretically, further loading should be accompanied with rapid load drop due to buckling of the honeycomb cell walls, but it not observed due to implemented material model for reduced model (solid volume with plasticity behaviour). In all cases where full model and reduced model obtained curves were compared, full model curves have significal drop in load carrying capacity to the next stable level (plateau). Damage reduction of 99% was used during the current study, but with an additional study it can be revised to lower values or different values of degradation that can be applied for fiber/matrix tension/compression stiffness degradation.

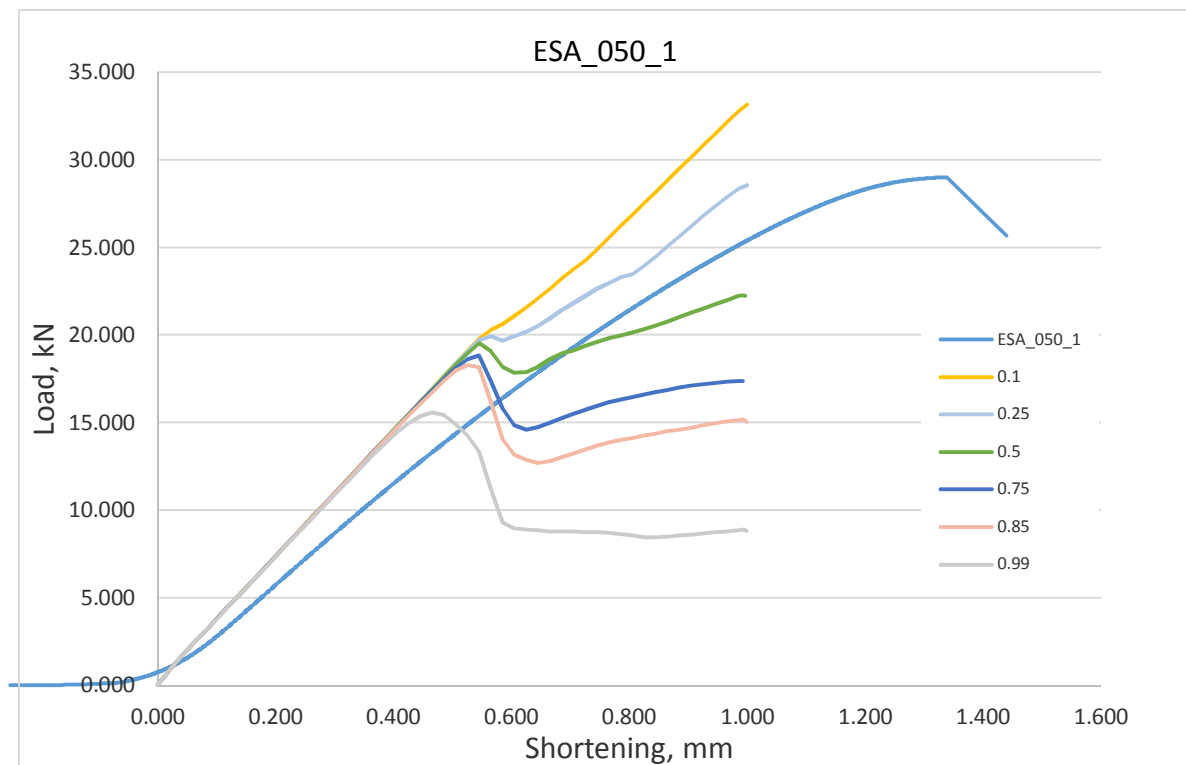


Figure 1.21. Simulation of different degree of degradation for ESA_050_1.

1.5 Boundary conditions and loading

Two type of boundary conditions corresponding to certain type of numerical model analysis were considered. Indentation (IND) and compression after impact (CAI) finite element analyses steps requires different boundary conditions. Depending on the loading stage boundary conditions were introduced as simply supportive around perimeter in case of indentation, simulating support of the indentation frame (restricting translation of the bottom face sheet in direction of

indentation (UZ) in combination with fixed individual nodes in the middle of the panel edges to restrict panel of free motion in in-plane direction (UY), which can cause numerical instability and restricting all of the nodes on one of the panel edges (UX). In case of edgewise compressive loading both longitudinal panel edges in depth of 20 mm was clamped, excluding the loading edge, where loading was introduced on master node of the coupled loading edge.

Load introduction for the indentation step (IND) was setup as solution time stepping dependent variable. Loading (Time=0.5) and unloading (Time=1.0) within one loadstep, so that at the end of loadstep (Time=1.0) indenter has moved double amount of indentation off the panel surface, to avoid contact with the panel surface in case of outward buckled skin. Indentation by displacement was considered as most appropriate way of load introduction because of the difference in stiffness response of two selected models. Total amount of deformation for both model was defined as discrete stiffness independent displacement of the indenter body. In case of direct load application, different models (different material properties in combination with specific finite element mesh density) can produce errors in terms of final deformation amount. In other words, direct application of indentation load should be avoided for both numerical and experimental analyses, due to different response of the structure. In case of experimental study, indentation by load will produce different dimples within the same series of panels, due to variation in stiffness (skin thickness variation, underlying honeycomb structure location variation, adhesive layer variation, etc.). In case of numerical study, final indentation depth of the different models (full model or reduced), will be stiffness dependent (material properties, mesh density, mathematical inconsistency of iterative solver, etc.), finally will produce large scatter of residual indentation.

Load introduction for the edgewise compression or compression after impact (CAI) step, was considered as displacement controllable, due to same reasons as for indentation step. Load carrying capacity was extracted from solution as reaction force on the master node of coupled support edge.

Large displacement non-linear analyses solution with accompanying solver options should be used. The major advantage of the reduced model is faster solution time and less problematic solution run (almost complete “unconvergent solutions” free solution). Solution controls should be adjusted according to solution needs. Automatic time stepping, and additional solver features for reduced model can be set as defaults. Two consecutive load steps should be prepared in terms of solution controls, boundary conditions, material properties, loading, etc. In case of Full model increased attention should be paid to solution controls related to convergence problems related with nonlinear solution of buckling of the honeycomb cell walls. Energy stabilization (used in current study) or damping stabilization techniques should be turned on, to overcome convergence problems related with bifurcation and reverse buckling during unloading stage. Several runs with specific amount of stabilization should be done to achieve convergence. As a basic value for energy stabilization used in the current study was, ratio of dissipated energy of $5e-3$. Stabilization should be used for both Indentation and CAI steps. Due to high computation costs of solution of full model, only several specimen models were solved for both Indentation and CAI step. Some additionally solved for indentation step only, mainly for comparison reasons, featuring increased mesh density.

1.6 Mesh sensitivity analyses

Mesh sensitivity analyses was performed with the focus on the most accurate representation of indentation shape and size. Since full 3D finite element model mesh size was dictated by the mesh ability to produce buckling of the honeycomb wall under indenter pressure, at least 2 elements per honeycomb cell side (1.5 mm for 3.2 mm cell and 2.0 mm for 6.4 mm) was considered as a minimum desired mesh. Finer mesh was not considered as an option due to high computational costs. As the basis of the finite element mesh for the reduced model was considered the same size as for full 3D model (1.5 mm). Additionally, mesh sensitivity analyses for coarser mesh were performed. Figure 1.22. shows indentation geometry and depth for four different mesh size. It was obvious that the most accurate shape and depth representation was observed for mesh size of 1.5 mm, in terms of shape curvature and indentation depth compared to experimental measurements, carried out by laser sensor. It was observed that for small size indenter (20 mm diameter), indentation depth and area diameter for load of indentation of 500 N, ranges with in: 0.41 - 0.48 mm indentation depth and 16.1 – 18.4 mm indentation area diameter. In other words, 8 mm per indentation half wave. That's mean that minimum number of elements needed for accurate indentation shape representation with 8-node shell elements (SHELL281), must be at least 4, to avoid formation of sharp angle between elements at the tip of the indentation and transition to the flat surface of the panel. Coarse mesh will likely produce diamond shaped indentation with sharp tip or flat shaped indentation with flat tip, thus considerably reducing actual indentation size. Finer mesh densities (less than 1.5 mm) was not considered, due to high computational cost.

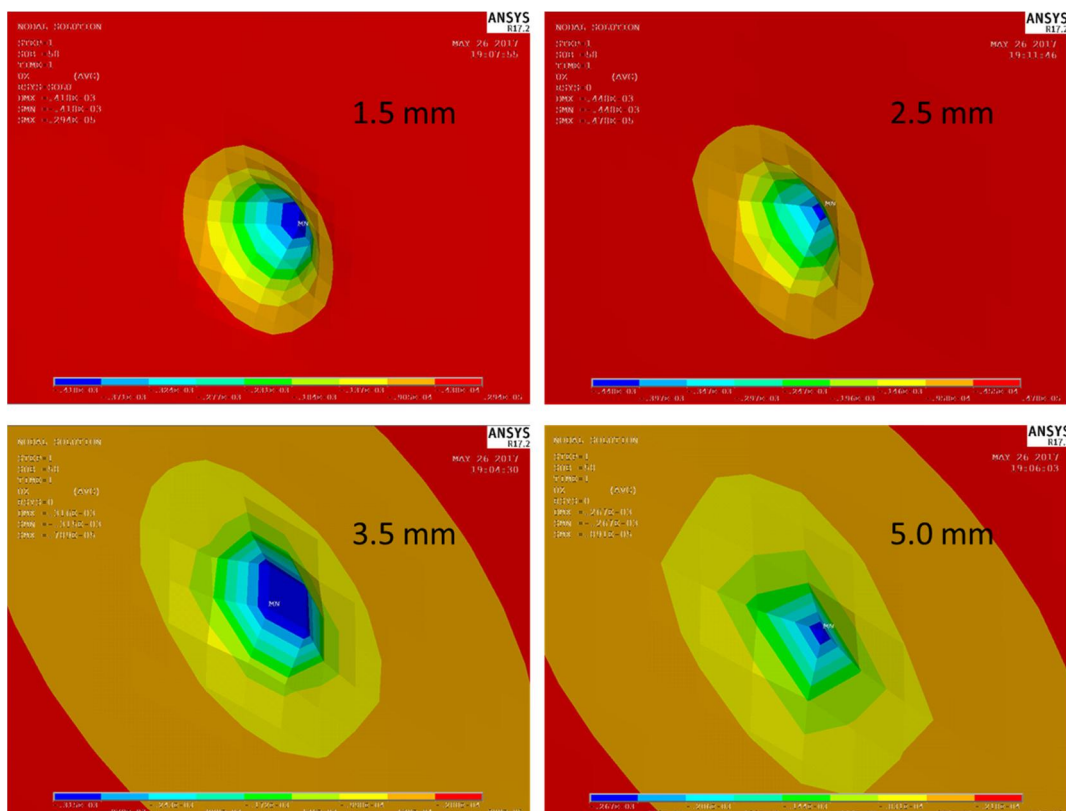


Figure 1.22. Indentation representation for different mesh density.

Figure 1.23., shows dependency of the calculated load carrying capacities depending on selected mesh density. It was seen that despite much lower indentation depth calculated for coarser mesh densities, there was not observed considerable increase in load carrying capacities compared to basic model (1.5 mm). That's mean that despite about 36% lower indentation depth (5 mm mesh density), load carrying capacity increased only by about 4 %, see Table 1.4. Where considerable decrease of depth of indentation observed for coarse mesh, will not produce considerable increase in load carrying capacity, Fig. 1.23, compared to experimental values, which are taken as first sign of failure values, which are equivalent to final model failure due to composite damage. It indicates that indentation depth for the current panel configuration was not the key factor for considerable load carrying capacity decreasing.

Table 1.4. Indentation depth and load carrying capacity.

	Indentation depth, mm	Load carrying capacity, kN
Exp.	0.41 - 0.48 (0.44 aver.)	9.854*
1.5 mm	0.418	9.149
2.5 mm	0.448	9.350
3.5 mm	0.315	9.527
5.0 mm	0.267	9.532

* - taking into account first sign of damage

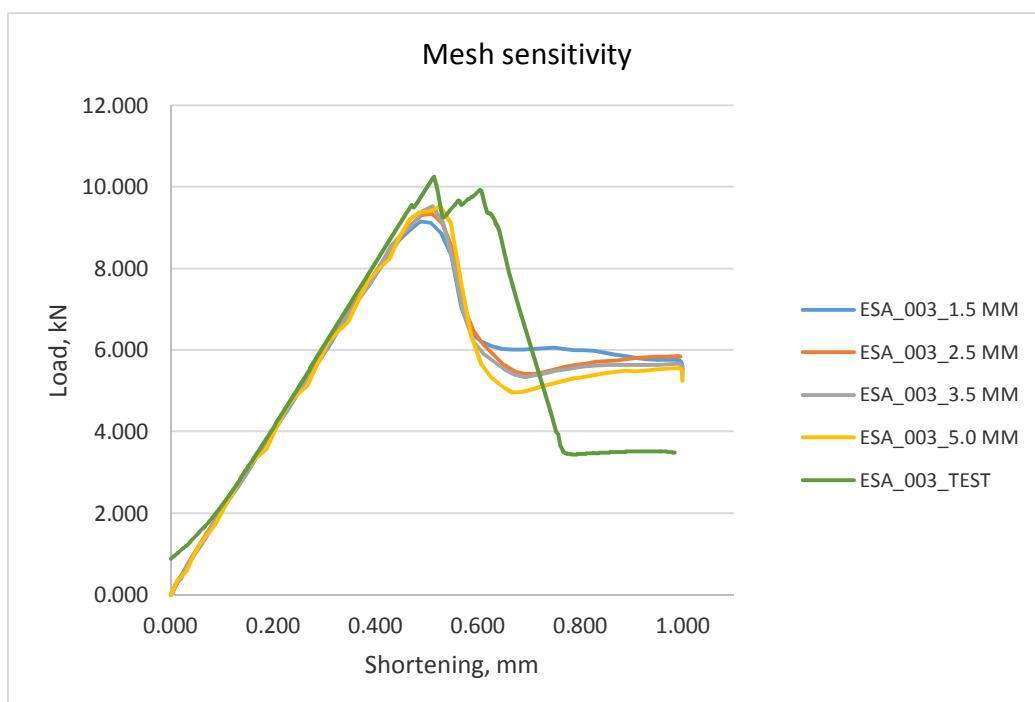


Figure 1.23. Mesh sensitivity analyses.

1.7 Plasticity model sensitivity analyses

Parametric adjustment of different plasticity material properties obtained from different sources was performed in the course of development of the reduced finite element model. Plasticity model of the honeycomb core was developed based on flatwise compression tests and adjusted to match experimentally measured indentation depth. Two step final element analyses were used. Stress values of honeycomb buckling (σ_B) and crushing stress (σ_{CR}) in combination with accompanying E_{core} modulus and E_{tan} tangent modulus, was used in finite element model for honeycomb structure material representation based on experimentally measured values. Stress value of honeycomb buckling was used for indentation (IND) step analyses, while crushing stress value was used for CAI analyses step. Some consideration on indentation loading and subsequent unloading stress-strain relationship can be considered based on honeycomb flatwise compression-tension experimental data. Different stress-strain model for unloading path can be included in model to increase precision of behaviour of the reduced model. This should be compared to fully functional full model, which should contain this effect through basic material properties model of aluminium honeycomb. Due to convergence problems, this was not possible to proof in current study.

1.8 References

1. ANSYS® *Academic Research, Release 16.2, Help System, Mechanical APDL Analysis Guide, ANSYS, Inc.*

2 Verification and validation of numerical approach

2.1 Validation of numerical models based on Indentation (IND) experiments

Comparison of two models in terms of skin damage propagation in comparison to experimental case as an example was shown for specimen ESA_027_5, Fig. 2.1. From the analyses of obtained progressive damage plots, Fig. 2.2 (Fiber tension failure, Matrix tension failure and Damage accumulation, showed as factor $0 < \text{damage} < 1$ for individual failure plots and ranging up to 2 for accumulation), can be seen that both models produced similar damage propagation patterns during indentation (IND) stage. At the same time all efforts by NDT detection of composite damage after impact not showed any sign of delamination in composite itself, rather delamination from adhesive layer, Fig. 2.3. Amount of residual indentation (dimple) at indenter unloading for both models were of the same order (1.45 and 1.32 mm for reduced and full model respectively), Fig. 2.4. Both models indicate both fiber and matrix failure in the location of indent. It should be noted that experimental specimen indentation scan showed much lower residual indentation than numerically obtained (0.7 mm). So in terms of damage propagation both, full model and reduced model showed good agreement in terms of composite damage, despite different residual indentation, which are of the same order, but still much higher than for experimental case.

Slightly larger damage area was observed for full model can be explained by discrete area (discrete cell step) of honeycomb structure underneath skin which support skin during indentation, while for reduced model there are continuous supporting structure underneath skin.

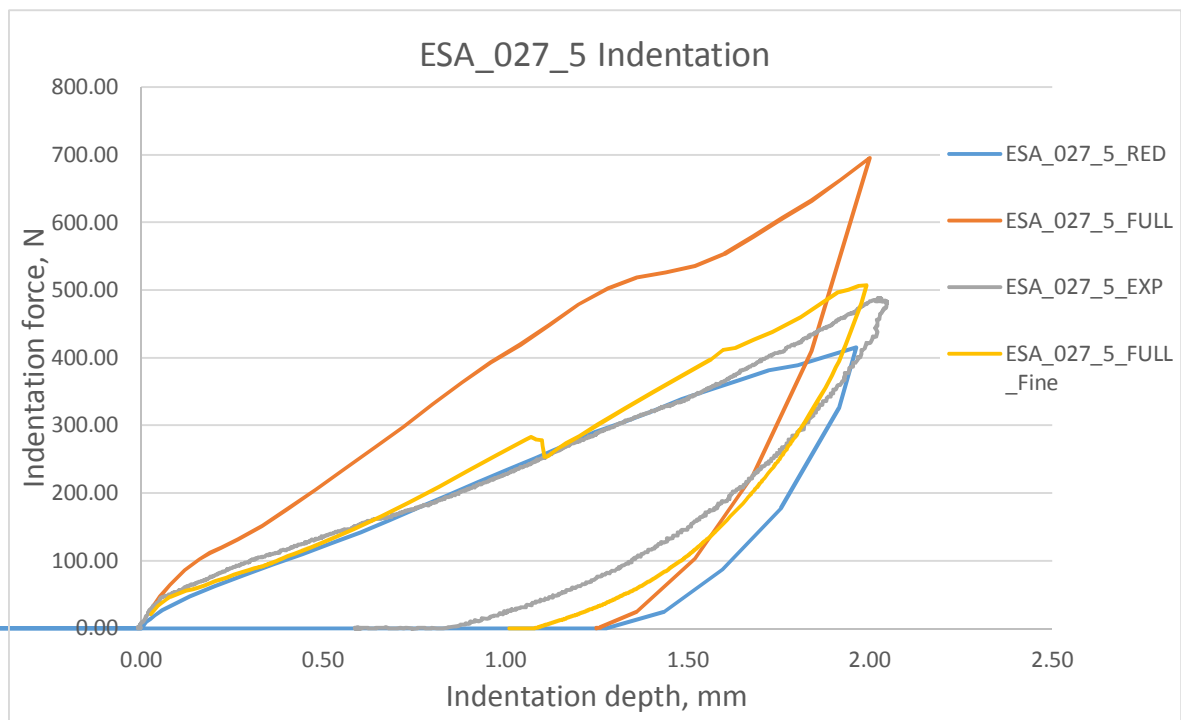


Figure 2.1. Indentation of ESA_027_5.

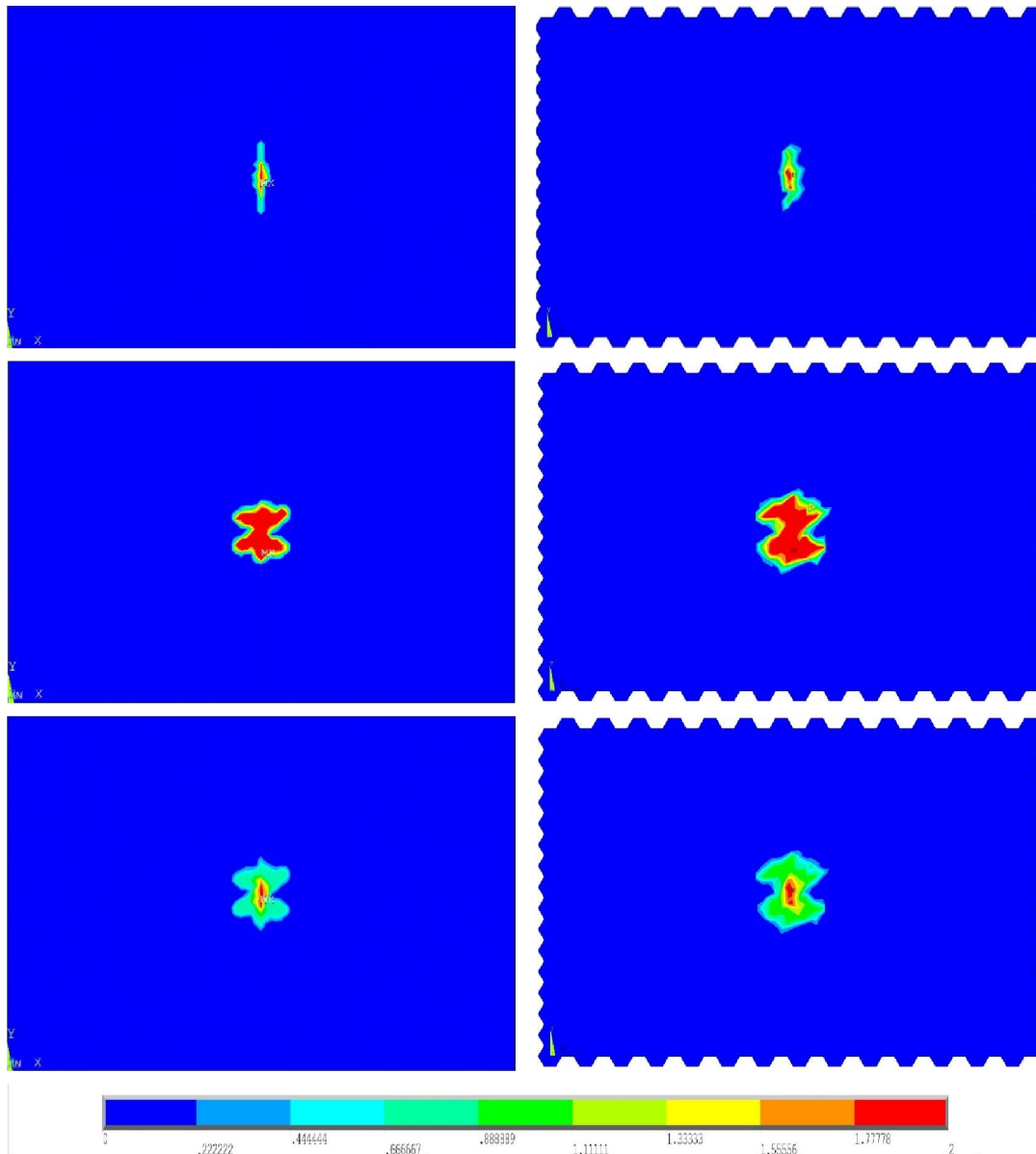


Figure 2.2. Composite fibre failure mode according to Max stress criteria.

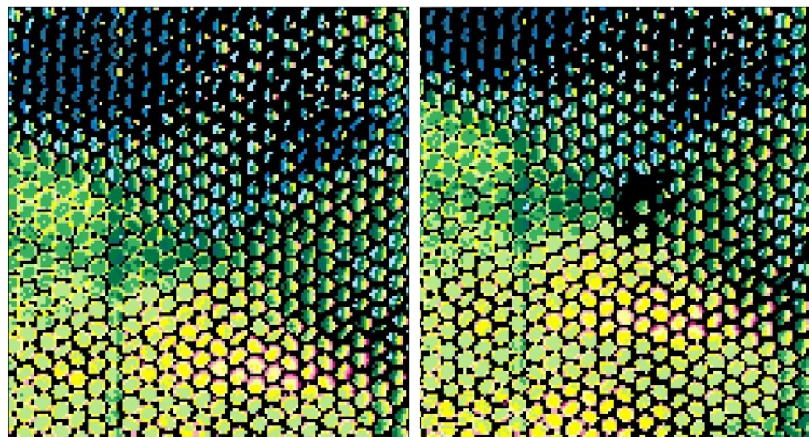


Figure 2.3. Composite fibre failure US scan before and after impact.

Almost all specimens covered by finite element analyses at the current study stage, showed much higher residual indentation in comparison to experimental study. Some additional study should be done addressing this particular issue.

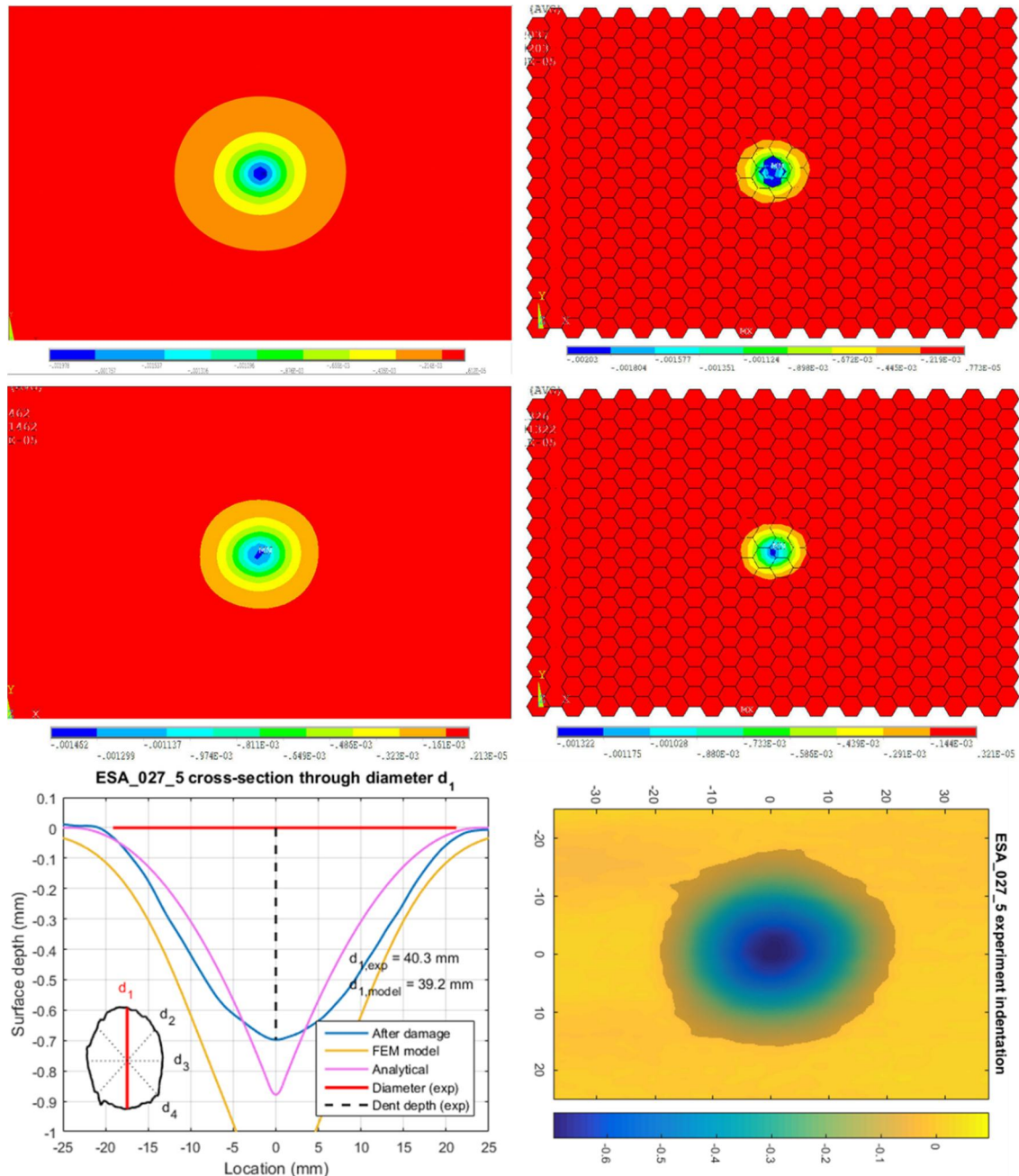


Figure 2.4. Residual indentation after impact.

2.2 Validation of numerical models based on CAI experiments

Validation of CAI experiments with finite element models (full model) showed good agreement with experimental results in terms of stiffness, Fig. 2.5. Obtained peak in load carrying capacity of numerical models (reduced model) indicates lower values

than experimental for vast majority of specimens, however in many cases (lower ply count especially), showed good correlation compared to experimental data (ESA_039, ESA_040 panels both 6.4 x 30 HC), Fig. 2.6. Numerical prediction of load carrying capacity for those panels was higher than experimentally obtained, Fig. 2.7.

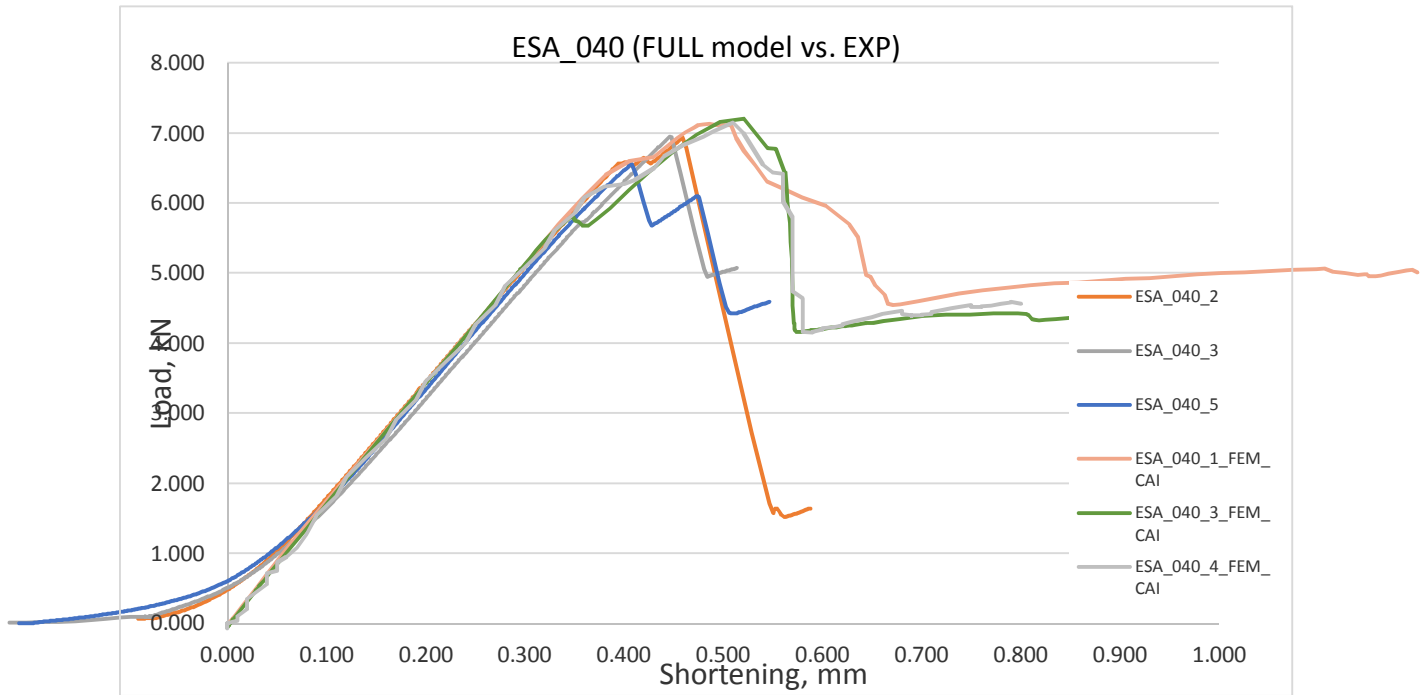


Figure 2.5. Comparison of full and reduced model stiffness for ESA_040 series.

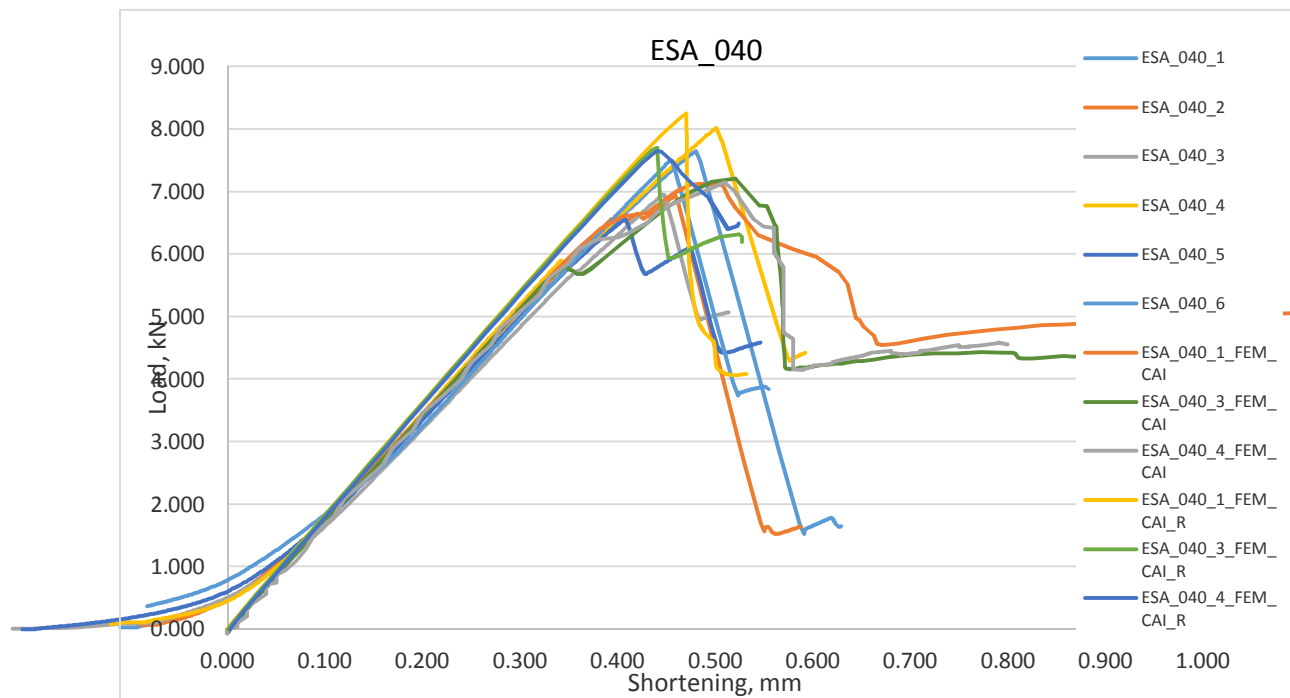


Figure 2.6. Experimental curves vs. FEM_CAI (Full model) and FEM_CAI_R (Reduced model).

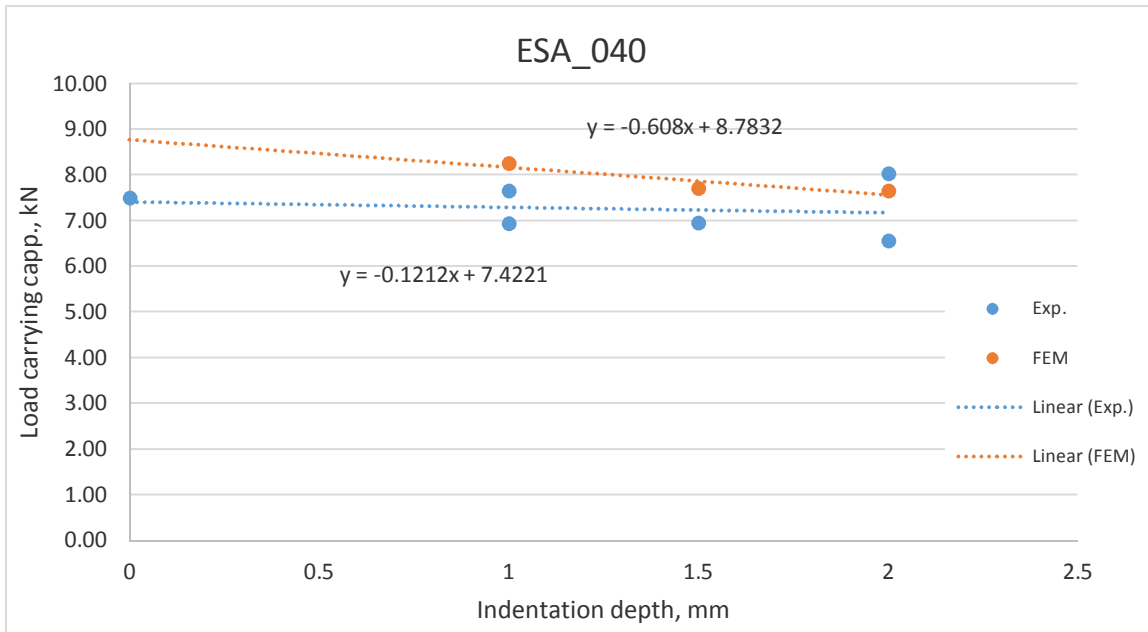


Figure 2.7. Numerical prediction (reduced model) vs. Experimental load carrying capacity ESA_040 series.

Some experimental specimens showed gradual damage propagation in form of non-significant load drops. This can be caused by face sheet delamination's or permanent damage accumulation, which probably not leading to permanent stiffness reduction, like it was identified by finite element model, but on sight of the first sign of degradation was still in good agreement with FEM model (ESA_041, 042, 043, 044 all as 3.2 x 20 and 3.2 x 30 HC). Fig. 2.8 – 2.11.

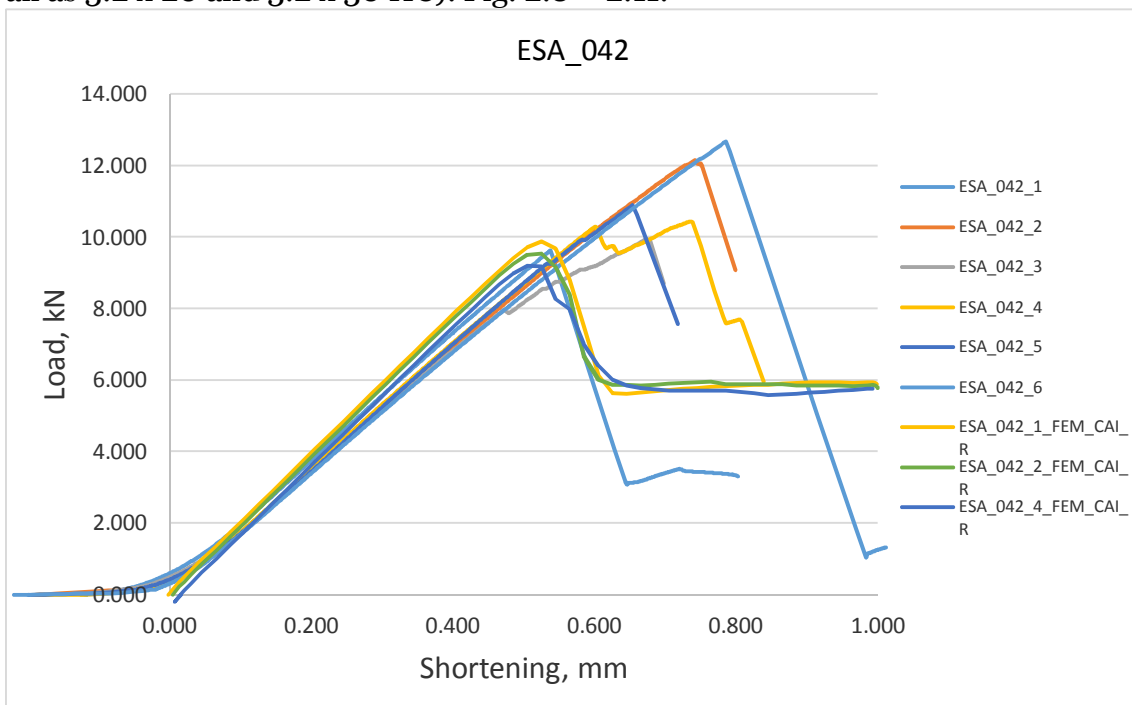


Figure 2.8. Numerical prediction (reduced model) vs. Experimental test curves ESA_042 series.

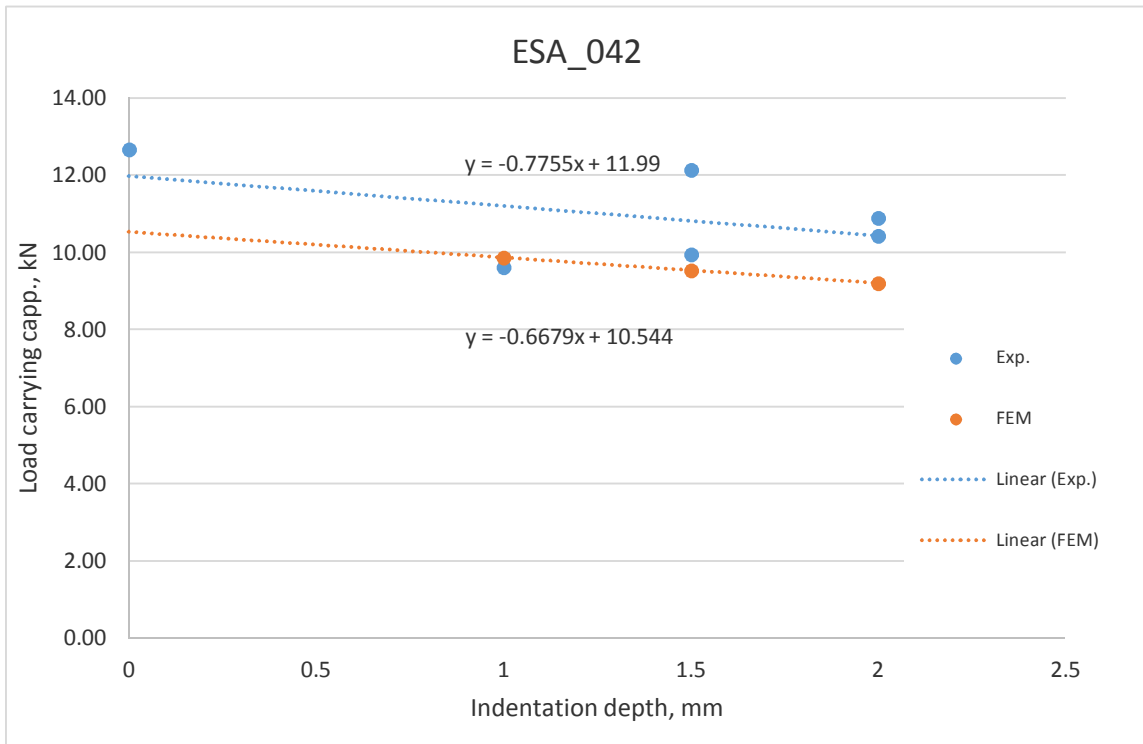


Figure 2.9. Numerical prediction (reduced model) vs. Experimental load carrying capacity ESA_042 series.

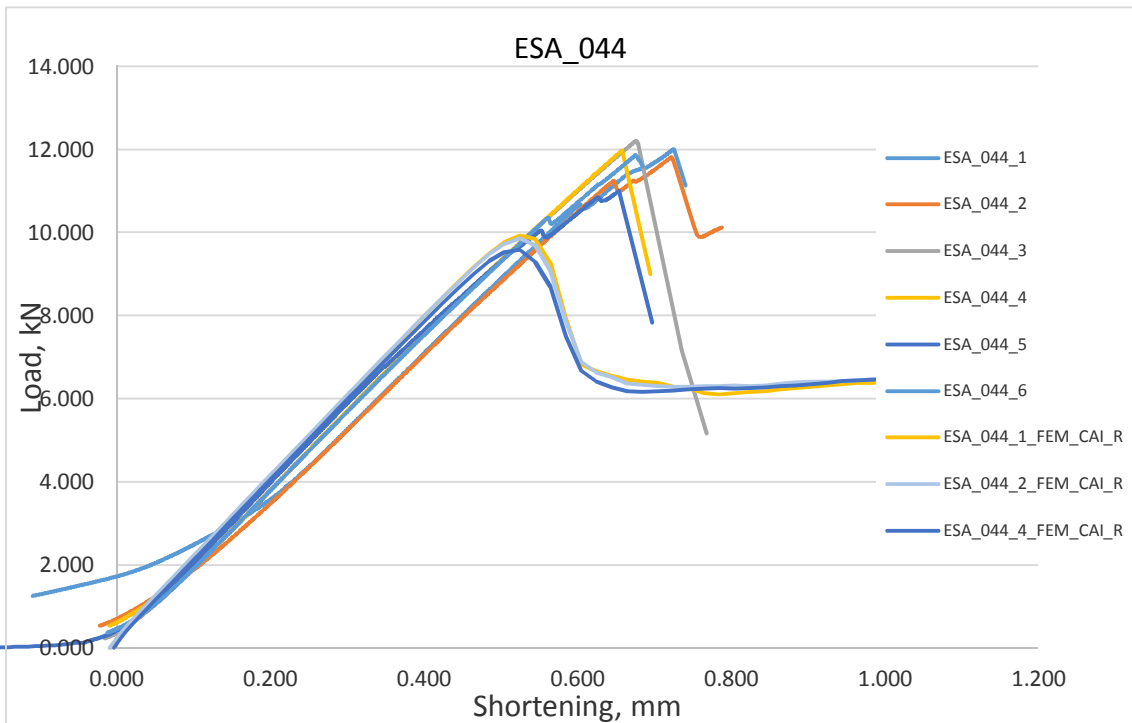


Figure 2.10. Numerical prediction (reduced model) vs. Experimental test curves ESA_044 series.

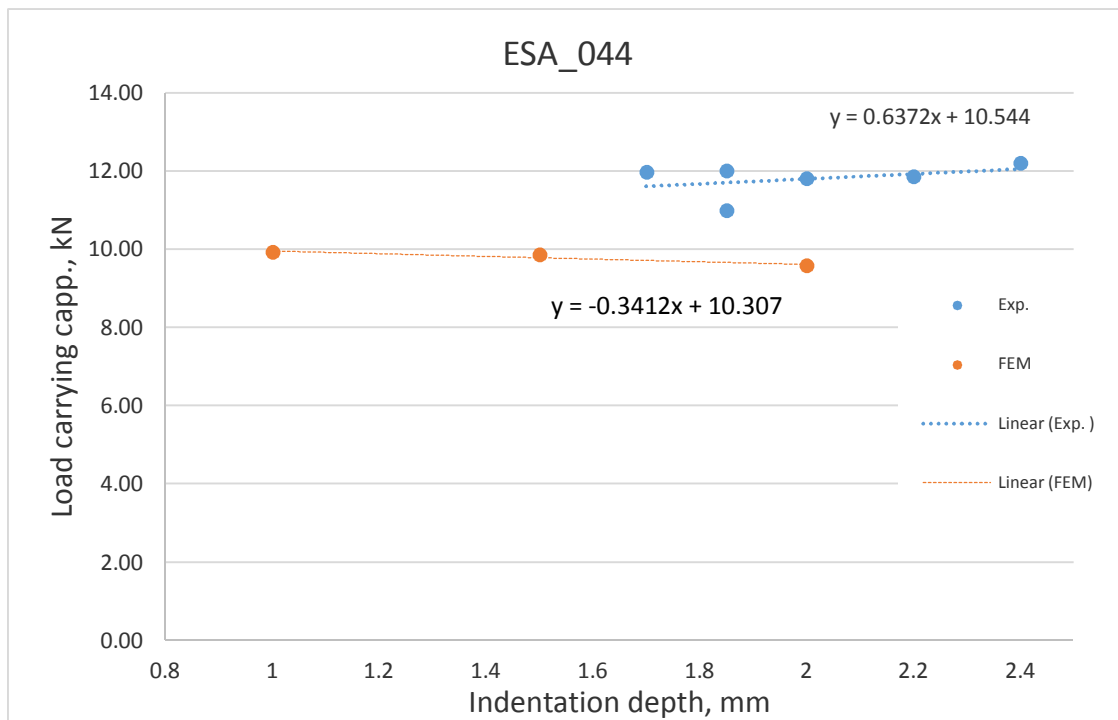


Figure 2.11. Numerical prediction (reduced model) vs. Experimental load carrying capacity ESA_044 series.

In most cases numerically predicted CAI load carrying capacity fell to lower bound of experimental data. This can be associated to numerical model designed failure due to material damage propagation and composite failure. In cases with 2 ply face sheet composite panel, failure can be predicted with good precision, while for thicker shells of 3 ply and especially 4 ply composite face sheet, only rare specimens were failed in good agreement with numerical model, for example Fig. 2.12, 2.13, ESA_037_3. Rather some compensation mechanism of higher number of plies worked against numerical ply failure criteria implemented in finite element model. Composite skin failure introduced by inward bending of the skin in region of indentation dimple, was less observed for 4 ply specimens due to presence of 0° layer on the inside surface of the skin.

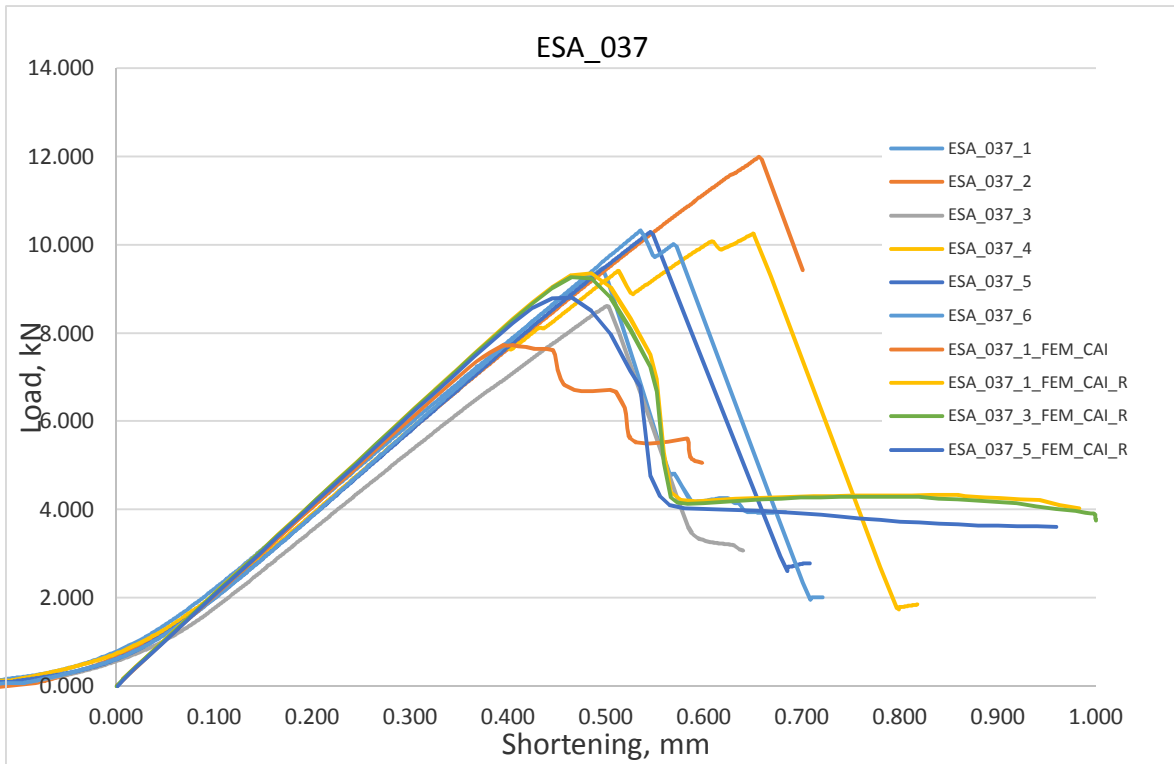


Figure 2.12. Numerical prediction (reduced model) vs. Experimental test curves ESA_037 series.

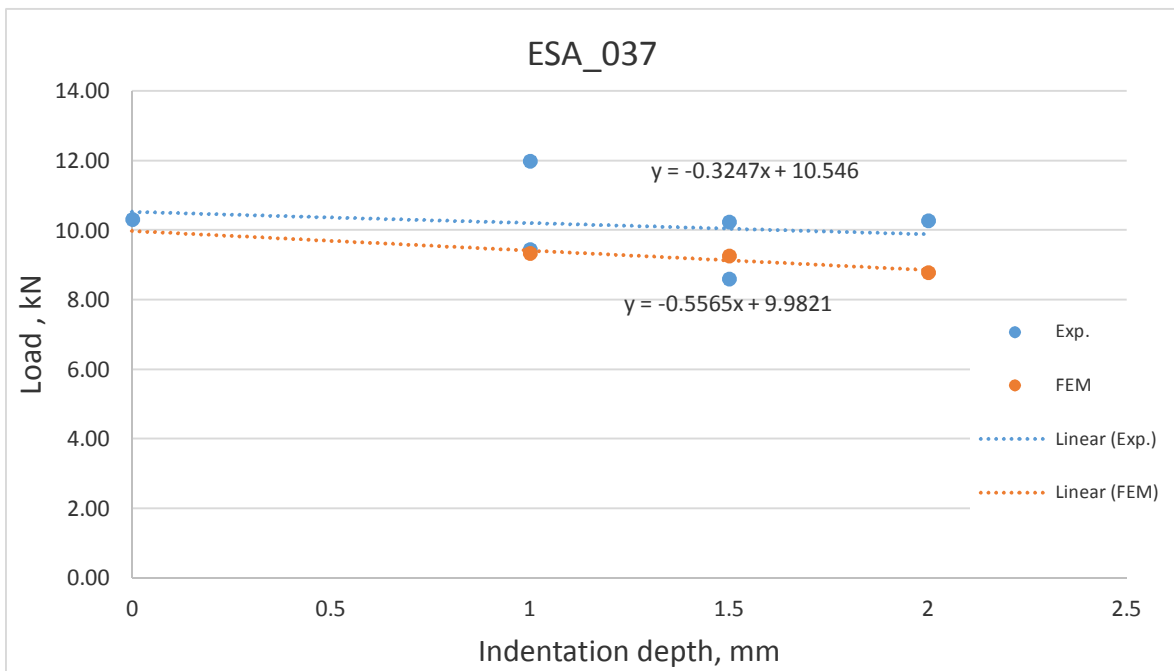


Figure 2.13. Numerical prediction (reduced model) vs. Experimental load carrying capacity ESA_037 series.

4 ply skin panels fell as well as all previously mentioned panels in two categories: 6.4 mm and 3.2 mm honeycomb cell size. 6.4 mm cell size panels has better agreement between numerical model and experimental data, Fig. 2.14, 2.15,

(ESA_028 and ESA_035), while some other showed differences in stiffness slope and much lower (about 1/3 ↓) carrying capacity (ESA_027 and ESA_034 according).

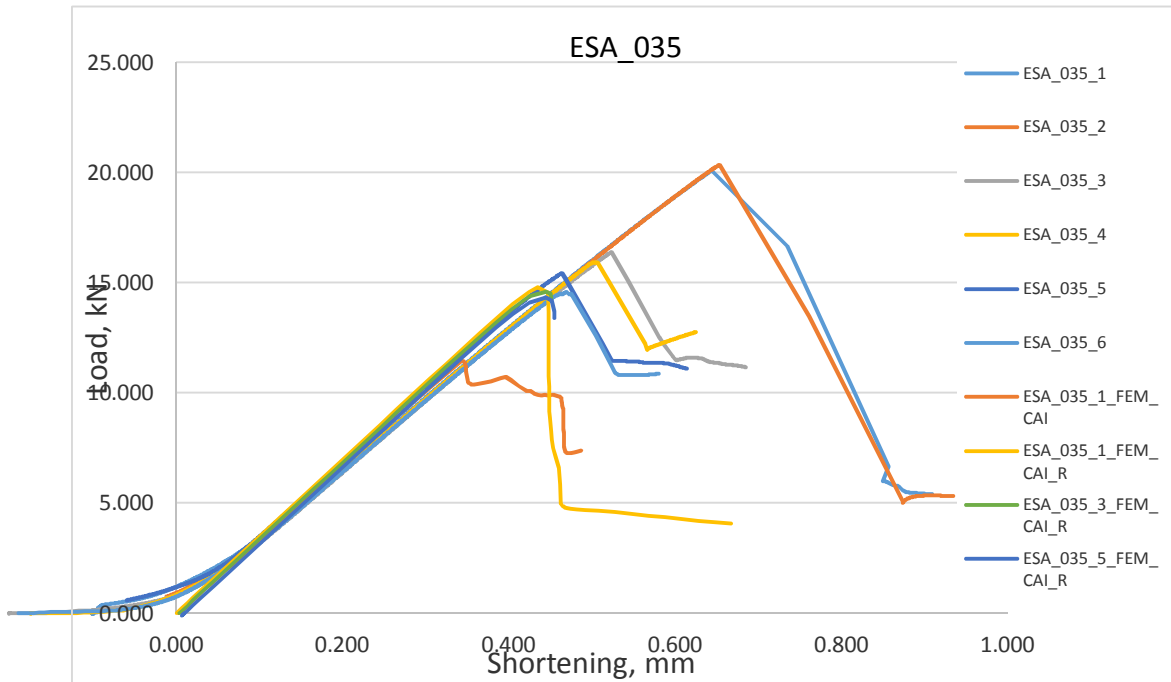


Figure 2.14. Numerical prediction (reduced model) vs. Experimental test curves ESA_035 series.

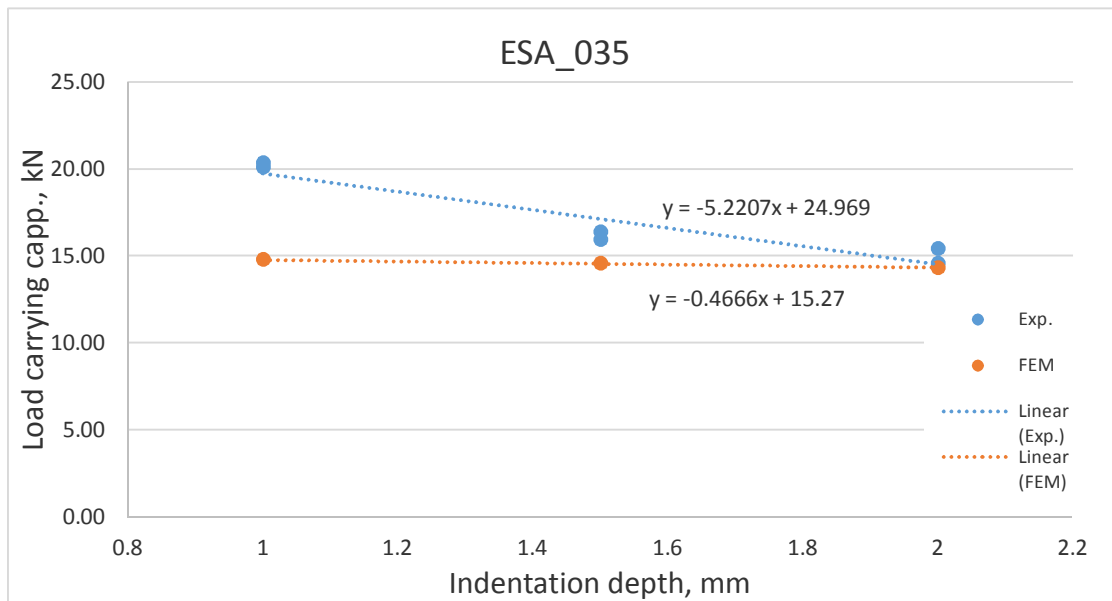


Figure 2.15. Numerical prediction (reduced model) vs. Experimental load carrying capacity ESA_035 series.

It should be noted that for the present experimental study panels having significant honeycomb stiffness in transverse direction (3.2 mm cell size honeycomb especially) are not sensitive to side impact imperfections, due to superior core density. Experimental maximum load carrying capacities indicates that there are different key factors that affect load values for individual specimens within series.

Numerical models for both 3.2 and 6.4 mm honeycomb cell size covered in this study indicates tendency to non-significant decrease of the load carrying capacity with the increase of residual indentation, which partially confirmed with experimental investigations, except for considerably lower predicted loads, especially for thicker face sheets. At the same time experimental data showed much higher scatter of data, including cases where panels with significant damage showed superior load carrying capacity than those of smaller damage or even those without damage. This can be explained by the low amount of statistical data or low quality (quality variation within series itself) of experimental specimens.

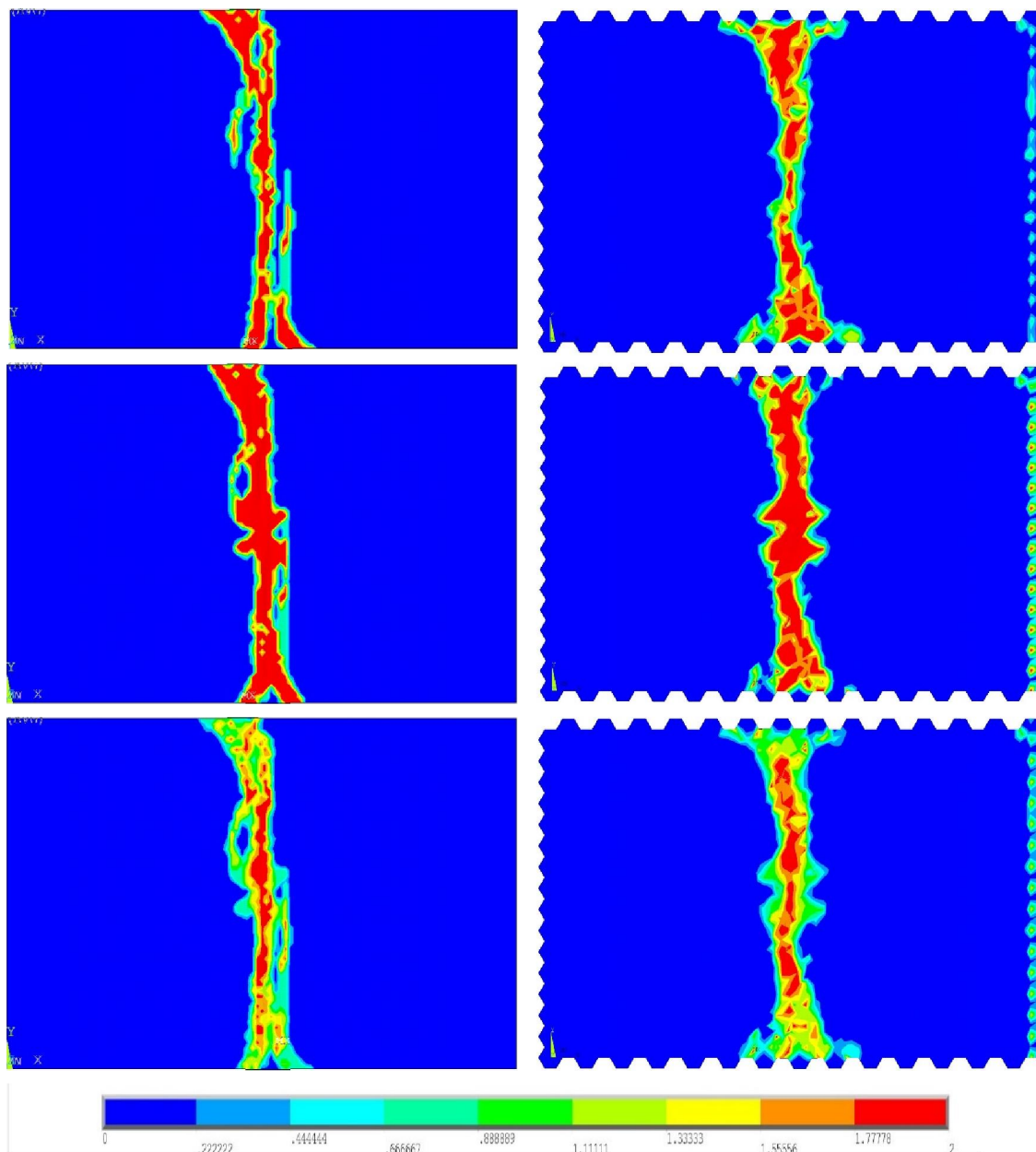


Figure 2.16. Composite fibre failure mode according to Max stress criteria, reduced model vs. full model, ESA_027_5.

Two model comparison in terms of skin damage propagation in comparison to experimental case as an example was shown for specimen ESA_027_5. From the analyses of obtained progressive damage plots can be seen that both model produce similar damage propagation patterns during CAI stage, Fig. 2.16. Amount of inward deflection at the end shortening of 1 mm for both models were of the same order (2.78 and 2.62 mm for reduced and full model respectively), Fig. 2.17. Both models indicate both fiber and matrix failure in the middle of the panel, while experimental specimen showed global skin inward buckling without visual skin breakage (typical for thick skin in combination with softer core). It should be noted that for other series experimental specimens exhibited with defined break of the skin in the middle of the panel (in combination with densier core).

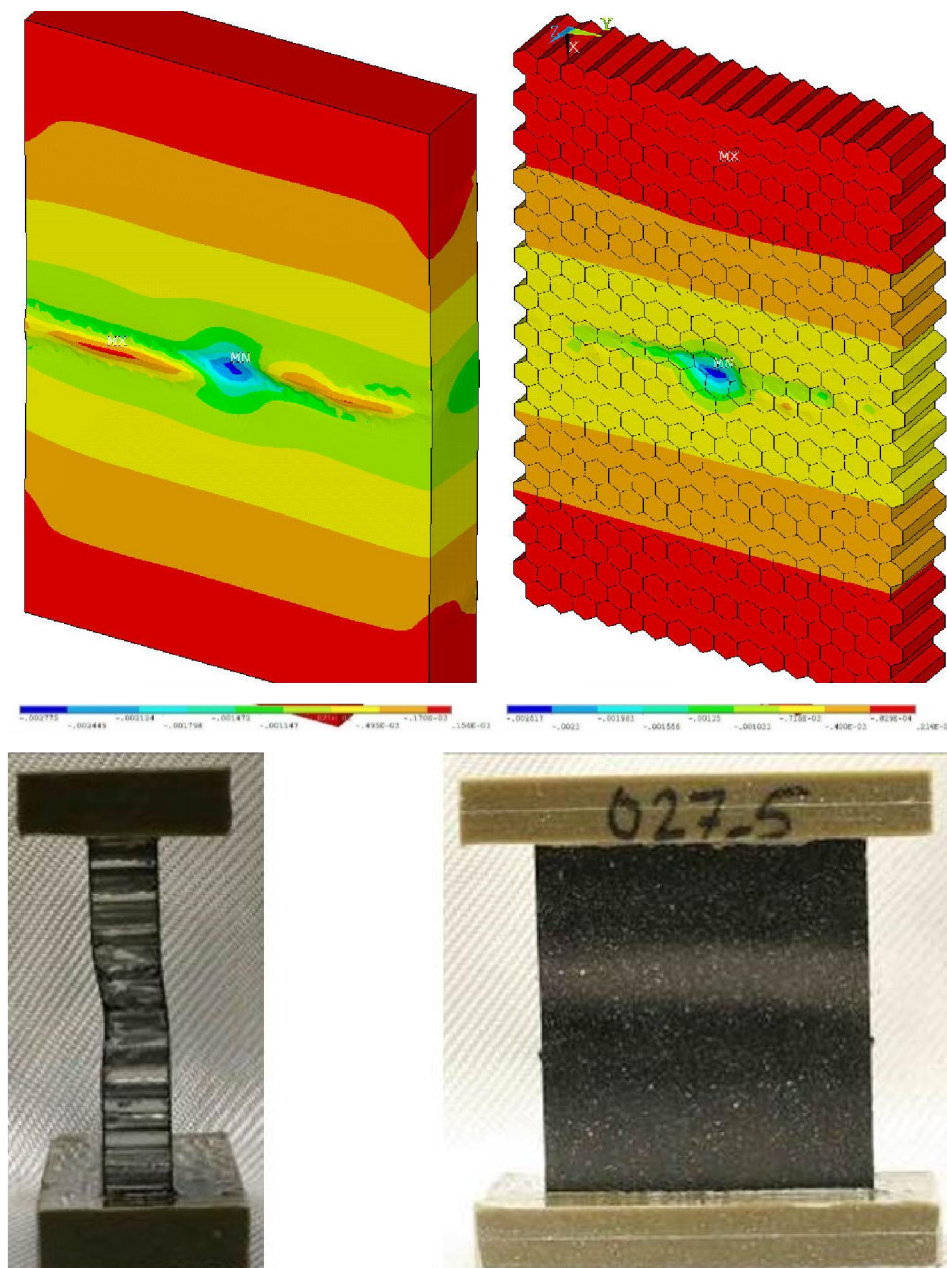


Figure 2.17. Numerical panel failure vs. experimental ESA_027_5.

2.3 Numerical model comparison with tested panels

Experimental compression after impact (CAI) tests on panels with three different lay-ups were carried out. Different lay-up configurations were considered with the aim of to find relationship between load carrying capacity and lay-up ply count, lay-up ply orientation order and honeycomb height.

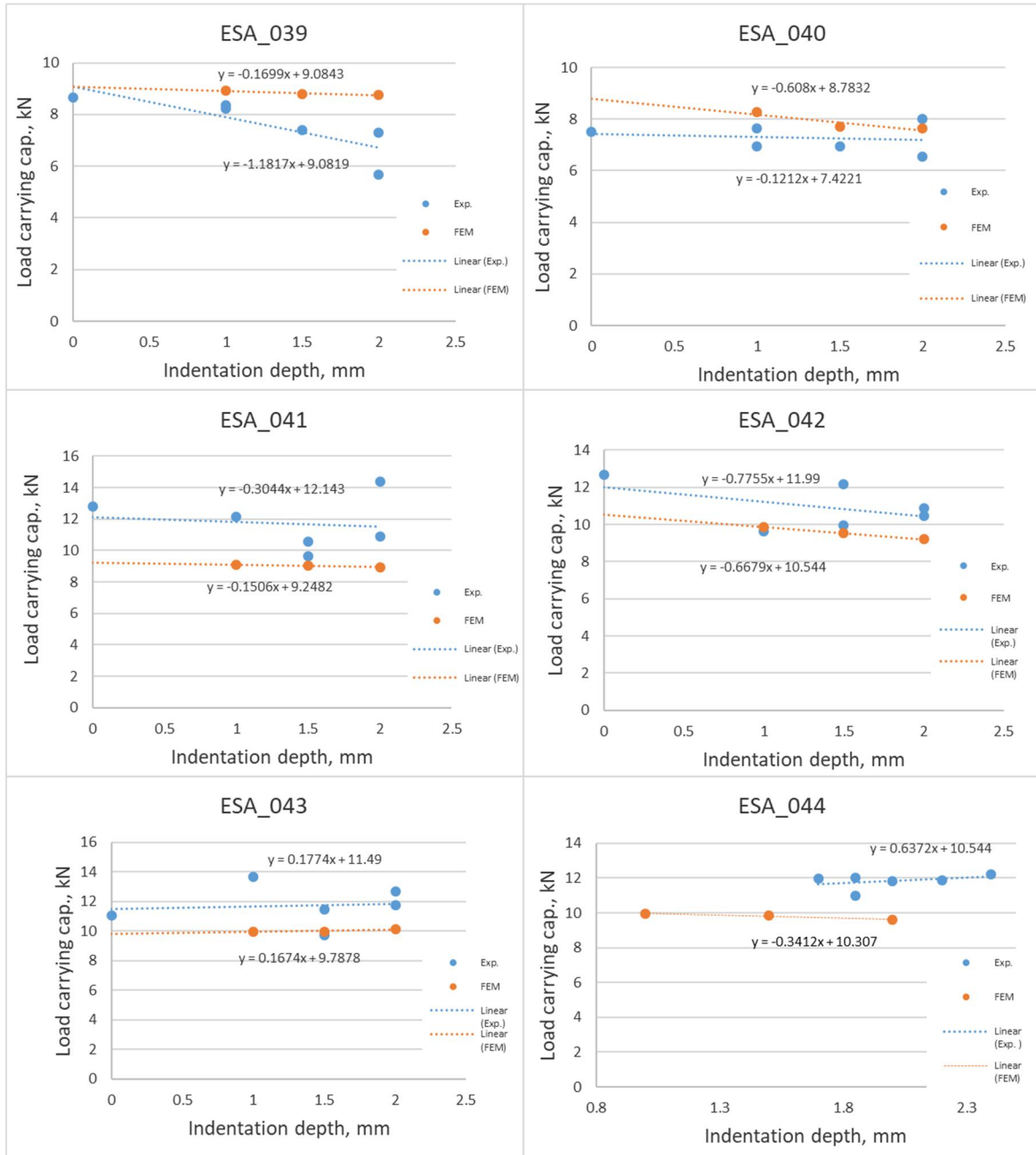


Figure 2.18. 2-ply panels with different HC density and thickness.

Fig. 2.18, shows finite element predictions in comparison to experimentally obtained data, for panels with 2-ply face sheets. Regardless honeycomb thickness (20 mm for ESA_041, 042 and 30 mm for ESA_043, 044) and indenter diameter (20 mm for ESA_041, 043, 044 and 150 mm for ESA_042, 044), all series of 3.2

mm cell size showed good correlation. Numerical prediction for those series was a bit lower than experiment, except some points, which matched very well. Softer honeycomb (6.4 mm cell size) (ESA_039 and ESA_040) showed that numerical predictions was slightly higher or was in close proximity with experimental results. Comparison of the expected numerical prediction for different indenter diameter, larger diameter indentation of the same depth produce less influence on the load carrying capacity for numerical prediction, while experimental data showed opposite effect.

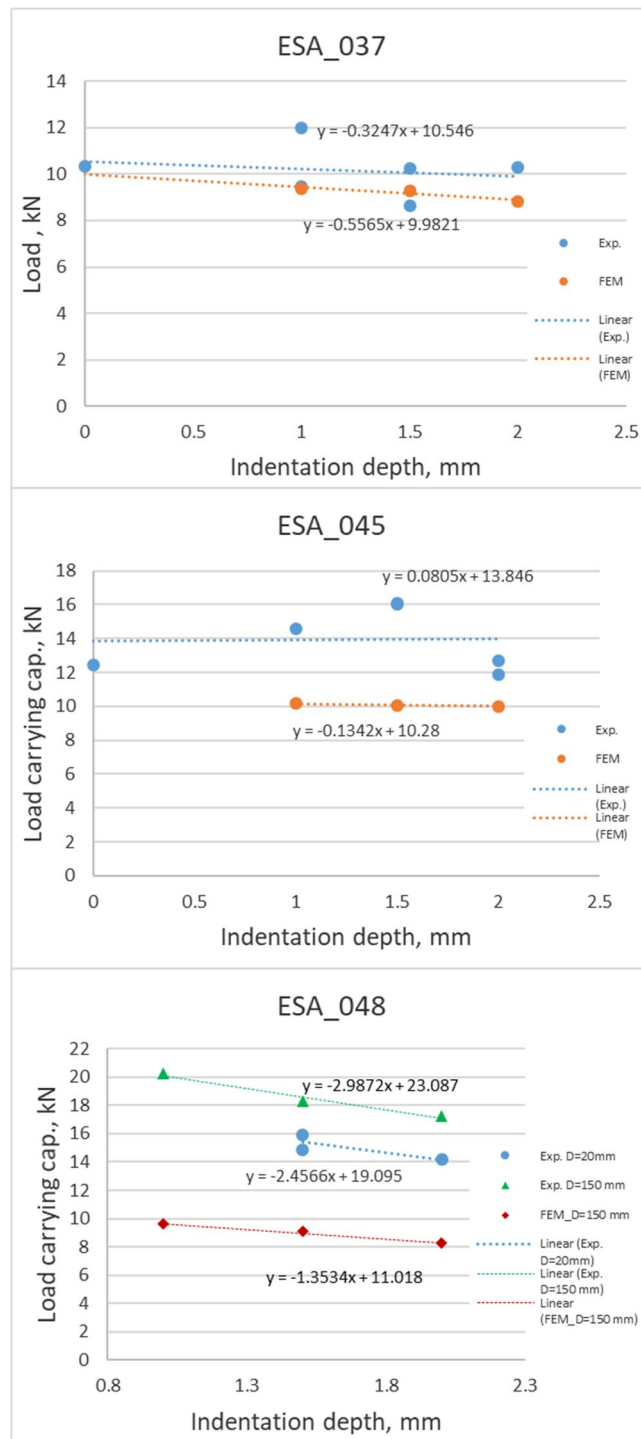


Figure 2.19. 3-ply panels with different HC density and thickness.

Fig. 2.19 shows numerical prediction for selection of 6.4 mm cell panel ESA_037 and 3.2 mm cell panels ESA_045 and ESA_048 with 3-ply face sheets. Numerical prediction of 6.4 mm cell honeycomb (ESA_037) was in good agreement with experimental results. While, 3.2 mm honeycomb showed considerably lower predicted loads, especially for larger indenter diameter (ESA_048).

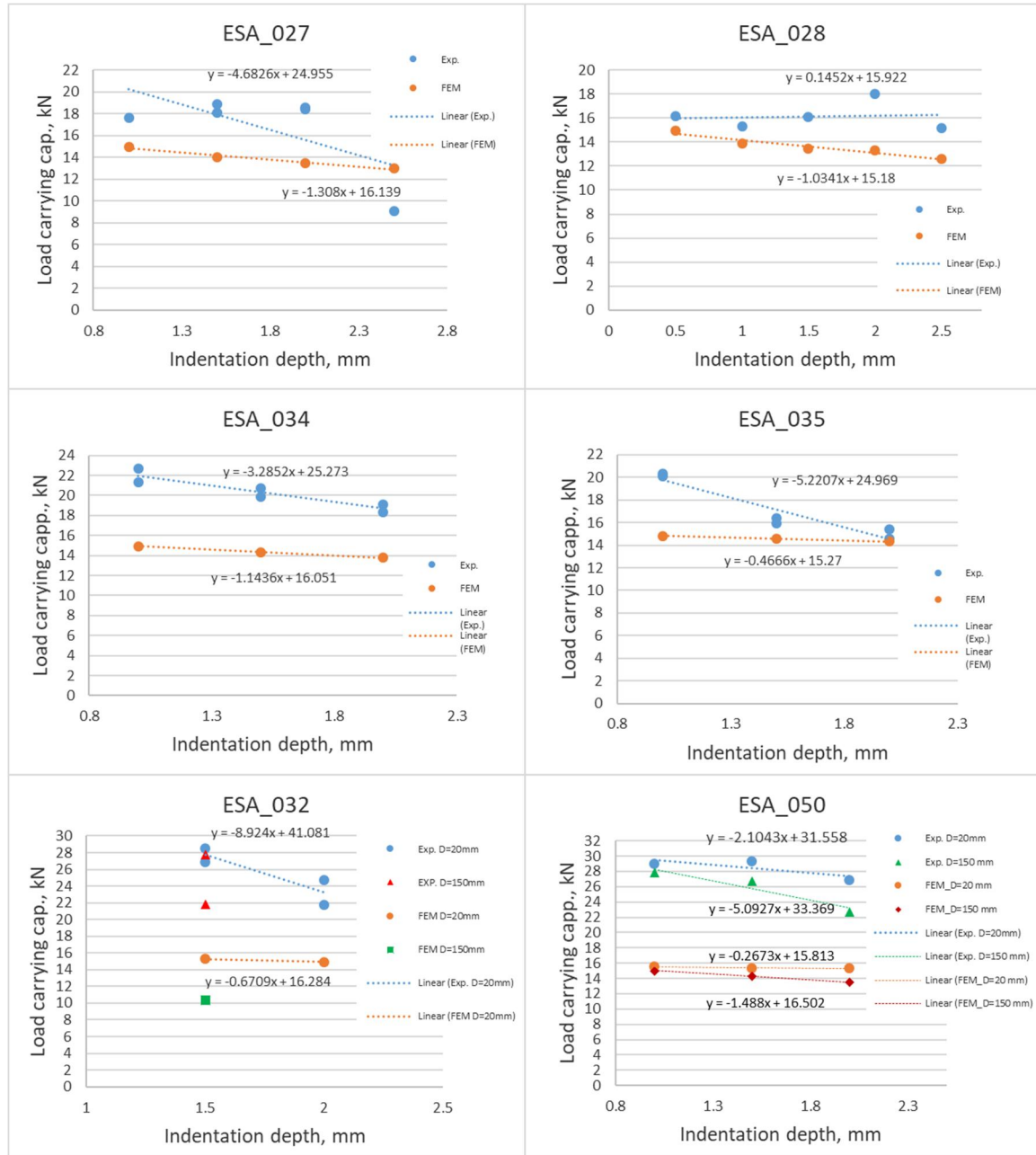


Figure 2.20. 4-ply panels with different HC density and thickness.

Fig. 2.20 shows numerical prediction for selection of 6.4 mm cell panels ESA_027, 028, 034, 035 and 3.2 mm cell panels ESA_032 and ESA_050 with 4-ply face sheets. Numerical prediction of 6.4 mm cell honeycomb (ESA_027 and ESA_028) regardless different indenter diameter was in good agreement with experimental results. While 30 mm thick honeycomb panels of the same configuration (ESA_034 and ESA_035), showed higher difference in predicted loads. Honeycomb panels

with 3.2 mm cell (ESA_032 and ESA_050), showed considerably lower predicted loads, but without any significant difference on indenter diameter.

Concluding comparison of numerical prediction of load carrying capacity with experimental tests it should be noted that in most cases numerical predictions showed linear relationship, in contrast to higher scatter of experimental data. Better predictions were obtained for softer honeycomb structure (larger cell size), than for denser structure. Additional studies on panel failure mode, relationship to honeycomb density covered in deliverable on experimental investigations.

3 Analytical model of residual indentation upon low-velocity impact of a sandwich panel

A characteristic mode of BVID in aluminium honeycomb core/CFRP facesheet sandwich structure is a dent left by the impactor, which is formed due to crushing and/or plastic deformation of the core. Such a residual indentation of a facesheet affects adversely the CAI strength of the sandwich by serving as a geometrical imperfection initiating inwards buckling of the facesheet and as a stress concentrator initiating facesheet fracture, see e.g. [1-3]. In either case, the reduction in CAI strength is directly related to the size and shape of the dent. Hence, an analytical tool for prediction of the residual dent geometry based on mechanical and geometrical characteristics of the sandwich and the impactor parameters would apparently be useful in, e.g., early design stages of a sandwich structure.

Most of the existing analytical models of low-velocity impact or quasi-static indentation applicable to Al honeycomb core/CFRP facesheet sandwich panels are focused primarily on the active loading, seeking to estimate maximum force and energy dissipated during impact [4-11], while only few consider the residual dent and its geometry, see e.g. [12]. In this section, an analytical model for quasi-static indentation of a sandwich panel by a hemispherical indenter [6, 12] is refined and extended to low-velocity impact loading of Al honeycomb/CFRP sandwich panels.

3.1 Load-indentation response

Consider quasi-static indentation of a rigidly supported composite sandwich by a rigid indenter, perpendicular to the facesheet surface, with a hemispherical tip of radius R . The geometrical model of facesheet displacement and the contact surface shown in Fig. 3.1 is based on that proposed in [6]: the surface S_1 corresponds to frictionless contact zone between the indenter and the facesheet, extending radially $0 \leq r \leq \rho$, where r is the radial coordinate of the polar coordinate system with origin at the axis of the indenter. S_2 designates free surface of the facesheet experiencing deflection due to indentation and extending within $\rho \leq r \leq a$, where a is the radius of indentation zone.

Neglecting the possible effect of the facesheet lay-up on geometry of the indentation, we assume that the dent is axially symmetric and deflection of the facesheet is function of the radial co-ordinate only, $w = w(r)$. The respective analytical expression for deflection is given by Eq. (1). Within the contact zone S_1 , $w(r)$ follows the geometry of the tip of the rigid indenter as proposed in [6]; displacement of the tip of indenter with respect to the unperturbed surface of the

facesheet is denoted by δ . The shape of deflection within zone S_2 is assumed such that $w(r)$ and $w'(r)$ are continuous at $r = \rho$ and deflection vanishes at $r = \rho$ smoothly, i.e. both $w(a) = 0$ and $w'(a) = 0$. Thus, refining the geometrical model of [6], we have hereby assumed a strictly axially symmetric deflection with $w = w(r)$ also in zone S_2 .

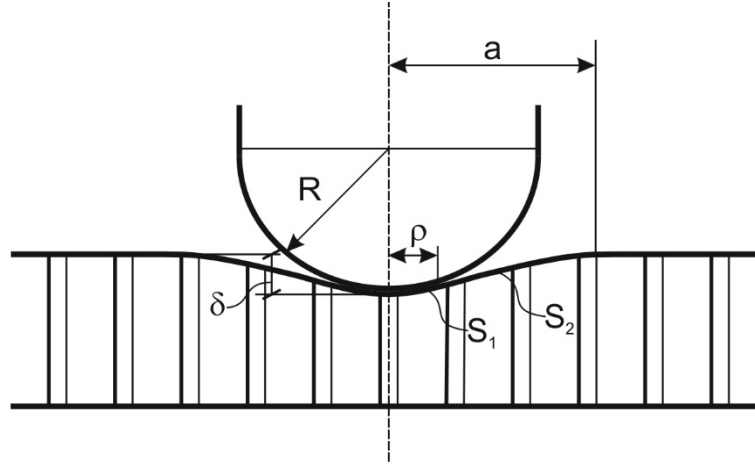


Figure 3.1 Schematic of indentation geometry.

$$w(r) = \begin{cases} \sqrt{R^2 - r^2} + \delta - R & 0 \leq r \leq \rho \\ \left(\sqrt{R^2 - \rho^2} + \delta - R \right) \left(1 - \frac{r - \rho}{a - \rho} \right)^2 & \rho \leq r \leq a \end{cases} \quad (1)$$

Continuity of the first derivative of $w(r)$, given by Eq. (1), at $r = \rho$ yields a constraint

$$\frac{\rho(a - \rho)}{2\sqrt{R^2 - \rho^2}} = \sqrt{R^2 - \rho^2} + \delta - R. \quad (2)$$

The total potential energy Π of the system schematically presented in Fig. 1 is

$$\Pi = U + D - W \quad (3)$$

where U stands for the elastic energy of the system, D denotes dissipated energy, and W is the work of external forces. The latter, for a given indentation force P and indenter displacement δ , is

$$W = P\delta \quad (4)$$

Appearance of the BVID implies that maximum displacement of the sandwich facesheet should exceed considerably its thickness. Then U can be approximated by

the elastic energy of the facesheet treated as a membrane, and D – by the work dissipated by plastic crushing of the core.

Areal strain energy density u of the facesheet in its axes of orthotropy is

$$u = \frac{1}{2} (A_{11}\varepsilon_{11}^2 + 2A_{12}\varepsilon_{11}\varepsilon_{22} + A_{22}\varepsilon_{22}^2 + A_{66}\varepsilon_{66}^2) \quad (5)$$

where A_{ij} are components of the stiffness matrix of the facesheet and ε_{ij} are the respective membrane strains. They are expressed via the facesheet deflection $w(r)$ as follows (see e.g. [11])

$$\begin{aligned} \varepsilon_{11} &= \frac{1}{2} \left(\frac{\partial w}{\partial r} \cos \varphi \right)^2 \\ \varepsilon_{22} &= \frac{1}{2} \left(\frac{\partial w}{\partial r} \sin \varphi \right)^2 \\ \varepsilon_{66} &= \frac{1}{2} \left(\frac{\partial w}{\partial r} \right)^2 \sin 2\varphi \end{aligned} \quad (6)$$

where φ is the angular coordinate in the polar coordinate system. Substituting Eqs. (1), (6) in Eq. (5) and integrating the latter in polar coordinates over zone S_1 , strain energy U_1 of the facesheet below the indenter is obtained as follows

$$U_1 = \int_0^{\rho} \int_0^{2\pi} u r d\varphi dr = \frac{\pi L}{64} \left[\frac{R^2 \rho^2}{R^2 - \rho^2} + \rho^2 + 2R^2 \log \left(1 - \frac{\rho^2}{R^2} \right) \right] \quad (7)$$

where $L = 3A_{11} + 2A_{12} + 3A_{22} + 4A_{66}$. In the same way, strain energy U_2 of the facesheet beyond the contact surface, within zone S_2 , is evaluated

$$U_2 = \int_{\rho}^a \int_0^{2\pi} u r d\varphi dr = \frac{\pi L}{60} \frac{(a + 5\rho) \left(\sqrt{R^2 - \rho^2} + \delta - R \right)^4}{(a - \rho)^3}. \quad (8)$$

Deformation behavior of the honeycomb core in flatwise compression is assumed to be rigid-perfectly plastic with the yield limit equal to the crushing stress q of the core, as demonstrated to be sufficiently accurate by the previous research [4-10]. Then the energy dissipated by core crushing below the indenter, D_1 , and beyond it, D_2 , is estimated, respectively, as

$$D_1 = \int_0^{\rho} \int_0^{2\pi} q w r d\varphi dr = \frac{\pi q}{3} \left[2R^3 - 3(R - \delta)\rho^2 - 2(R^2 - \rho^2)^{3/2} \right] \quad (9)$$

and

$$D_2 = \int_{\rho_0}^a \int_0^{2\pi} q w r d\varphi dr = \frac{\pi q}{6} (a - \rho)(a + 3\rho) \left(\sqrt{R^2 - \rho^2} + \delta - R \right). \quad (10)$$

It follows from the derivations above that the potential energy Eq. (3) takes the form

$$\Pi = U_1 + U_2 + D_1 + D_2 - W. \quad (11)$$

Due to the geometrical constraint Eq. (2), only two of the quantities ρ , δ , a are independent. Expressing a from Eq. (2)

$$a = \rho + \frac{2}{\rho} \left(R^2 - \rho^2 - (R - \delta) \sqrt{R^2 - \rho^2} \right) \quad (12)$$

and substituting Eq. (12) into Eqs. (7)-(10), we finally obtain the potential energy Eq. (11) as $\Pi = \Pi(\delta, \rho)$:

$$\begin{aligned} \Pi(\delta, \rho) = & -P\delta + \frac{1}{64} \pi L \left(\frac{R^2 \rho^2}{R^2 - \rho^2} + \rho^2 + 2R^2 \log \left(1 - \frac{\rho^2}{R^2} \right) \right) + \\ & \frac{1}{240} \pi L \frac{\rho^2 \left(\sqrt{R^2 - \rho^2} - R + \delta \right)^4 \left(R^2 + 2\rho^2 - (R - \delta) \sqrt{R^2 - \rho^2} \right)}{\left(R^2 - \rho^2 - (R - \delta) \sqrt{R^2 - \rho^2} \right)^3} + \\ & \frac{1}{3} \pi q \left(2R^3 - 3(R - \delta) \rho^2 - 2(R^2 - \rho^2)^{3/2} \right) + \\ & \frac{2}{3} \pi q \frac{\left(\left(R^2 - (R - \delta) \sqrt{R^2 - \rho^2} \right)^2 - \rho^4 \right) \left(\sqrt{R^2 - \rho^2} - R + \delta \right)}{\rho^2} \end{aligned} \quad (13)$$

The indenter displacement δ and contact zone size ρ at a given applied force are obtained as the values minimizing the total potential energy, Eq. (13). This can be done by seeking the stationary point of $\Pi(\delta, \rho)$

$$\begin{cases} \frac{\partial \Pi(\delta, \rho)}{\partial \delta} = 0 \\ \frac{\partial \Pi(\delta, \rho)}{\partial \rho} = 0 \end{cases} \quad (14)$$

Although the first of the relations in Eq. (14) leads to an explicit expression for indentation force P in terms of indenter displacement δ and contact zone size ρ , the second relation still needs to be solved numerically. Alternatively, appropriate direct numerical minimization procedures can be applied to Eq. (13). Upon evaluation of δ and ρ , indentation radius a is obtained from Eq. (12).

3.2 Indentation under low-velocity impact

Estimation of the maximum dent depth δ during low-velocity impact by a rigid indenter, perpendicular to the facesheet surface, with a hemispherical tip of radius R is based on the following simplifying assumptions. First, kinetic energy W of the impactor is assumed to be spent only on denting the sandwich; then it is equal to the work of indentation $\int_0^{\delta} P(x)dx$ where $P(x)$ is the indentation force as a function of indentation depth x . Further, indentation force-depth relation is linearized, $P(x) = kx$ (such an assumption is used for simplification in the sandwich impact analysis to enable analytical solution, see e.g. [13]). This leads to $\int_0^{\delta} P(x)dx = P(\delta)\delta/2$. Hence the relation of impact energy and maximum indentation depth takes the form $W = P(\delta)\delta/2$ for low-velocity impact case. The dent depth δ and contact zone size ρ at a given impact energy W are obtained as the values minimizing the total potential energy, Eq. (13), and simultaneously fulfilling the condition given by Eq. (15):

$$W = \frac{P\delta}{2}. \quad (15)$$

Having thus determined the maximum dent depth δ and contact zone size ρ , dent radius is evaluated using Eq. (12).

Neglecting the part of impact energy spent on global bending of the sandwich panel during impact results in some overestimation of dent size. Similarly, applying composite facesheet stiffness characteristics and core crushing stress, as obtained in quasi-static loading, in low-velocity impact analysis also should cause slight overestimation of the dent. Such an overestimation of BVID appears acceptable because it is likely to lead to conservative estimates of the residual load bearing capacity of the sandwich.

3.3 Residual indentation

Consider unloading of the panel which has been indented either quasi-statically or by low-velocity impact. During unloading, the indented facesheet partially rebounds. We make a simplifying assumption that the extent of BVID zone, characterized by its radius a , and overall shape Eq. (1) do not change during unloading as shown schematically in Fig. 3.2, and the geometrical constraint Eq. (2) also holds.

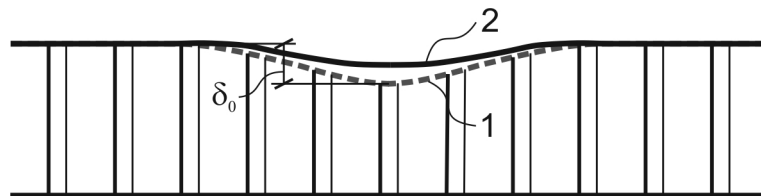


Figure 3.2 Schematic of indentation profiles at the end of active loading (1) and upon unloading (2).

The residual indentation depth upon unloading is evaluated by minimizing the potential energy at zero indentation load as suggested in [14] and allowing for the work of core unloading stress q_{ct} as described in [12]. The potential energy upon complete unloading (i.e. when $P = 0$) is expressed as

$$\Pi = U_r + D . \quad (16)$$

In Eq. (16), D is the work of plastic deformation of the core during unloading and U_r denotes the residual deformation energy of the facesheet. Designating the unloading yield stress of the core (called also core restoring pressure [12]) by q_{ct} , denoting the indentation profile at the end of active loading by w_0 , and the residual indentation profile by w_r , the dissipated energy is expressed as

$$D = q_{ct} \int_0^a \int_0^{2\pi} (w_0 - w_r) r d\phi dr . \quad (17)$$

Core unloading stress (also called core restoring pressure [12]) is core yield strength in unloading, and it characterises the energy dissipation in the core during unloading of the sandwich. Note that core crushing stress q and unloading yield stress q_{ct} need not be equal for a given core. q_{ct} can be determined experimentally as the plateau level of the tensile stress in flatwise tension-after-compression test of the honeycomb core, while the compressive plateau stress in this test is the core crushing stress q .

Both indentation profiles in Eq. (17) comply with Eq. (1), but for w_0 indentation depth δ_0 and contact zone radius ρ_0 reached at the end of active loading have to be used in Eq. (1), while for w_r - the residual values δ_r , ρ_r of the respective indent characteristics. Upon integration and substitution of indenter displacement by an expression following from Eq. (2)

$$\delta = \frac{2R\sqrt{R^2 - \rho^2} - 2R^2 + \rho(a + \rho)}{2\sqrt{R^2 - \rho^2}} , \quad (18)$$

we finally obtain

$$D = \frac{1}{12} \pi q_{ct} \frac{-8R^4 + 4R^2 \rho_0^2 + 8R^3 \sqrt{R^2 - \rho_0^2} + \rho_0(a + \rho_0)(a^2 + \rho_0^2)}{\sqrt{R^2 - \rho_0^2}} - \frac{1}{12} \pi q_{ct} \frac{-8R^4 + 4R^2 \rho_r^2 + 8R^3 \sqrt{R^2 - \rho_r^2} + \rho_r(a + \rho_r)(a^2 + \rho_r^2)}{\sqrt{R^2 - \rho_r^2}} \quad (19)$$

Similarly, the expression of residual strain energy is obtained from Eqs. (7), (8) upon substitution of Eq. (18) and of the respective contact zone radius value, leading to

$$U_r = \frac{1}{64} \pi L \left(\frac{R^2 \rho_r^2}{R^2 - \rho_r^2} + \rho_r^2 + 2R^2 \log \left(1 - \frac{\rho_r^2}{R^2} \right) \right) + \frac{1}{960} \pi L \frac{\rho_r^4 (a - \rho_r)(a + 5\rho_r)}{(R^2 - \rho_r^2)^2} \quad (20)$$

Inserting the expressions Eqs. (19), (20) into Eq. (15), and dropping the first term of Eq. (19) because it is constant and so does not affect minimization of the potential energy with respect to ρ_r , we obtain $\Pi = \Pi(\rho_r)$ as follows

$$\Pi = \frac{1}{64} \pi L \left(\frac{R^2 \rho_r^2}{R^2 - \rho_r^2} + \rho_r^2 + 2R^2 \log \left(1 - \frac{\rho_r^2}{R^2} \right) \right) + \frac{1}{960} \pi L \frac{\rho_r^4 (a - \rho_r)(a + 5\rho_r)}{(R^2 - \rho_r^2)^2} - \frac{1}{12} \pi q_{ct} \frac{-8R^4 + 4R^2 \rho_r^2 + 8R^3 \sqrt{R^2 - \rho_r^2} + \rho_r (a + \rho_r)(a^2 + \rho_r^2)}{\sqrt{R^2 - \rho_r^2}} \quad (21)$$

Upon finding the value of ρ_r that minimizes the potential energy Π given by Eq. (21), depth of the residual dent can be evaluated from Eq. (18) as

$$\delta_r = \frac{2R \sqrt{R^2 - \rho_r^2} - 2R^2 + \rho_r (a + \rho_r)}{2 \sqrt{R^2 - \rho_r^2}} \quad (22)$$

3.4 Validation

The analytical model described above has been validated against test results of aluminium honeycomb core/CFRP facesheet sandwich specimens subjected to quasi-static indentation and low-velocity impact, and comparison of the analytically predicted and experimentally determined residual dent cross-section geometries are presented in http://bnm4eks.rtu.lv/tools_en.html. For analytical calculations of residual dent geometry, previously obtained UD composite properties, crushing stress q of Al honeycombs determined by flatwise compression tests and core unloading stress q_{ct} evaluated from flatwise tension-after-compression tests were used.

As a representative example, experimentally determined and predicted dent cross-section geometries are presented in Fig. 3.3 for sandwiches with (a) [0/90] facesheet lay-up and 6.4/20 mm core subjected to quasi-static indentation at 125 N force by a hemi-spherical indenter with 20 mm tip diameter and (b) [-60/60/0] facesheet lay-up and 6.4/30 mm core subjected to low-velocity impact of 0.49 J energy by a hemi-spherical indenter with 20 mm tip diameter. The crush and unloading stress values for these honeycombs were evaluated at $q = 0.35$ MPa and

$q_{ct} = 0.13$ MPa. The overall agreement of predicted and measured residual dent shape appears reasonable in Fig.3.3, while the dent diameter is overestimated.

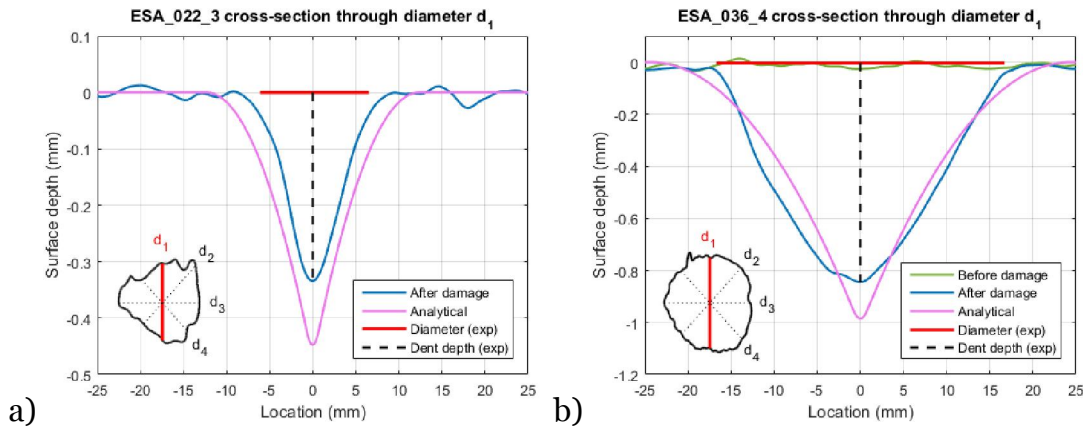


Figure 3.3 Experimentally determined (“After damage”) and predicted (Analytical) dent cross-section geometries for sandwich coupons with [0/90] facesheet lay-up upon quasi-static indentation (a) and [-60/60/0] facesheet lay-up upon low-velocity impact (b).

As another example of indentation behavior, Fig. 3.4 shows maximum indentation depth (i.e. indentation at the end of the active loading phase) and residual dent depth (a), as well as dent diameter (b), as functions of the maximum indentation load for sandwiches with facesheet lay-up [0/90] and 3.2/20 mm core. The crush and unloading stress values for these honeycombs were evaluated at $q = 1.05$ MPa and $q_{ct} = 0.5$ MPa. The indentation was performed by an indenter having a hemi-spherical tip with 150 mm diameter.

The sandwich coupons were supported only along their perimeter during indentation test by placing a coupon on a steel frame. Therefore, apart from the local deformation at the indenter, the sandwich also underwent global deformation by bending and shear. It has been demonstrated in, e.g., [6, 7, 9, 10], that the indenter tip displacement (equal to the top facesheet displacement under indenter) δ_A , in such a case can be represented as a sum of indentation depth and the global deflection of the sandwich (equal to the bottom facesheet displacement under indenter) δ_B . Since both top and bottom facesheet displacements along the line of indentation were recorded during the tests with frame support of sandwich specimens, the experimental indentation depth at the maximum load was evaluated as

$$\Delta\delta = \delta_A - \delta_B$$

and the respective values plotted in Fig. 3.3a.

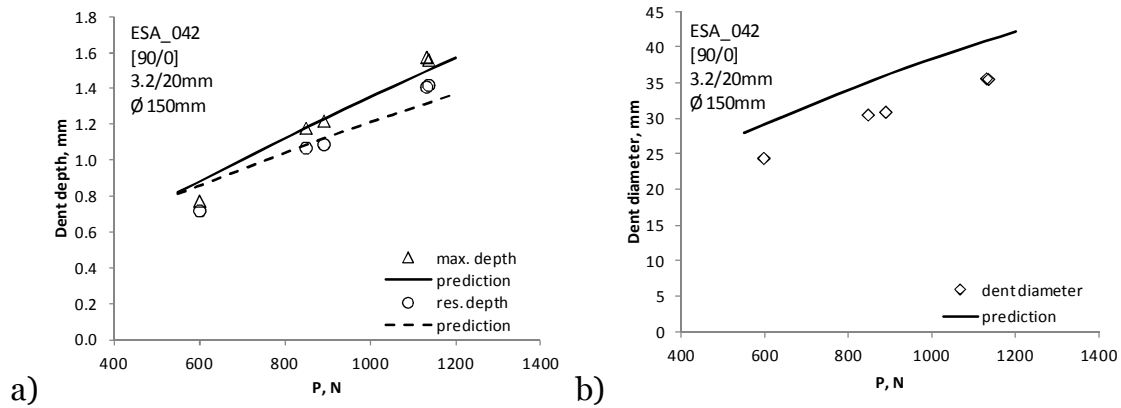


Figure 3.4. Maximum indentation depth, residual dent depth (a) and dent diameter (b) for sandwich coupons with [0/90] facesheet lay-up in quasi-static indentation as functions of maximum indentation load.

In Fig. 3.5, residual dent depth (a) and dent diameter (b) are presented as functions of the low-velocity impact energy W for sandwich coupons with facesheet lay-up [0/60/-60/0] and 6.4/20 mm core. The impactor had a hemi-spherical tip with 20 mm diameter.

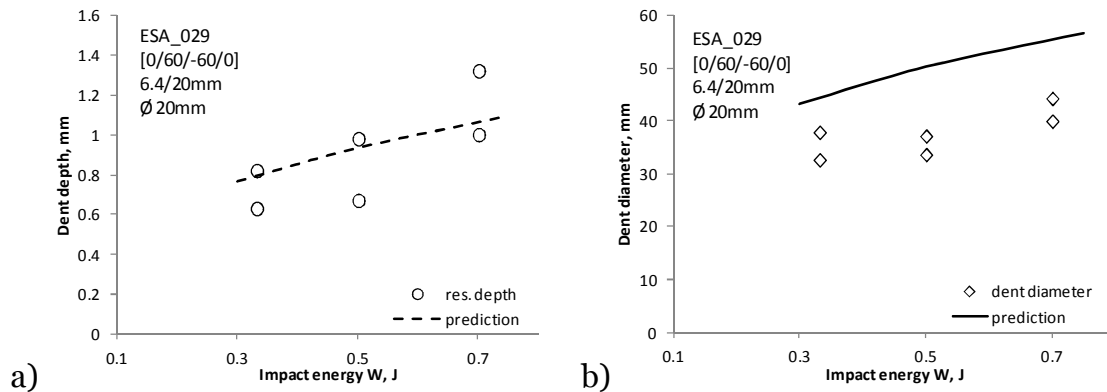


Figure 3.5 Residual dent depth (a) and dent diameter (b) for sandwich coupons with [0/60/-60/0] facesheet lay-up upon low-velocity impact as functions of impact energy.

It is seen from the data presented in http://bnm4eks.rtu.lv/tools_en.html and in Figs. 3.3-3.5 above that the analytical model developed captures the overall profile of the residual dent reasonably well both for quasi-static and low-velocity impact loading of sandwich coupons. The predicted dent diameter, while mostly close to the experimental values, is consistently overestimated. Thus, the model tends to overestimate the extent of impact damage, which is likely to lead to a conservative CAI strength estimate based on the theoretical dent profile.

3.5 References

1. Cvitkovich MK, Jackson WC. Compressive Failure Mechanisms in Composite Sandwich Structures. *Journal of the American Helicopter Society* 1999;44(4):260–268.
2. Kalnins K, Graham AJ, Sinnema G. Verification of residual strength properties from compression after impact tests on thin CFRP skin, Al honeycomb composites (2012) European Space Agency, (Special Publication) ESA SP, 691 SP, 7 p.
3. Czabaj MW, Zehnder AT, Davidson BD, Singh AK. Compressive strength of honeycomb stiffened graphite/epoxy sandwich panels with barely-visible indentation damage. *Journal of Composite Materials* 2014; 48(20):2455–2471.
4. Türk MH, Hoo Fatt MS. Localized damage response of composite sandwich plates. *Composites: Part B* 1999;30:157–165.
5. Hoo Fatt MS, Park KS. Dynamic models for low-velocity impact damage of composite sandwich panels – Part A: Deformation. *Composite Structures* 2001;52: 335–351.
6. Lin C, Hoo Fatt MS. Perforation of Sandwich Panels with Honeycomb Cores by Hemispherical-nose Projectiles. *Journal of Sandwich Structures and Materials* 2005;7(2):133–172.
7. Lin C, Hoo Fatt MS. Perforation of Composite Plates and Sandwich Panels under Quasi-static and Projectile Loading. *Journal of Composite Materials* 2006;40:1801-1840.
8. Chai GB, Zhu S. A review of low-velocity impact on sandwich structures. *Proceedings of the Institution of Mechanical Engineers, Part L: Journal of Materials Design and Applications* 2011;225:207-230.
9. Khalili SMR, Hosseini M, Fard KM, Forooghy SH. Static indentation response of an in-plane prestressed composite sandwich plate subjected to a rigid blunted indenter. *European Journal of Mechanics A/Solids* 2013;38:59-69.
10. Fard KM, Khalili SMR, Forooghy SH, Hosseini M. Low velocity transverse impact response of a composite sandwich plate subjected to a rigid blunted cylindrical impactor. *Composites: Part B* 2014;63:111–122.
11. Feli S, Khodadadian S, Safari M. A modified new analytical model for low-velocity impact response of circular composite sandwich panels. *Journal of Sandwich Structures and Materials* 2016;18(5):552–578.
12. Singh AK, Davidson BD, Zehnder AT, Hasseldine BPJ. An analytical model for the response of carbon/epoxy-aluminum honeycomb core sandwich structures under quasi-static indentation loading. In: *Proceedings of the American Society for Composites - 31st Technical Conference, ASC, 2016*.
13. Malekzadeh Fard K, Khalili SMR, Forooghy SH, Hosseini M. Low velocity transverse impact response of a composite sandwich plate subjected to a rigid blunted cylindrical impactor. *Composites: Part B* 2014;63:111–122.
14. Zenkert D, Shipsha A, Persson K. Static Indentation and Unloading Response of Sandwich Beams. *Composites: Part B* 2004;35:511–522.

4 Analytical estimation of CAI strength of a sandwich with BVID

4.1 Analytical estimation of CAI strength of a sandwich with BVID

For an analytical model of residual strength of an impact-damaged CFRP/AL sandwich to be useful in early design stages of sandwich structures, the model should provide relatively simple and tractable relations for CAI strength based on the characteristics of BVID, such as residual dent diameter and depth, that would nevertheless provide reasonably accurate, conservative strength estimate. For that, the failure mechanisms of a sandwich in CAI should be well understood and their principal features correctly reflected in the model. As recently summarized in [1] based on [2-8], the principal CAI failure mechanisms of sandwiches with BVID are:

- unstable propagation of the dent, preceded by gradual dent growth via progressive core crushing;
- unstable propagation of a kink band zone in the facesheet, originating at the dent in the stress concentration zone;
- compressive fiber failure;
- delamination buckling.

The CFRP/AL sandwich coupons studied in the current project, that failed in CAI due to BVID, exhibited mostly the first of the fracture mechanisms listed above, namely, they failed via unstable propagation of the dent, originating at the BVID, across the specimen width. Models of various complexities have been developed for prediction of the dent growth via such an inward-type buckling of the facesheet [7, 13-15]. Even those among them that are called analytical models [9-12] rely heavily on methods of numerical analysis such as fine discretization of the region to be modeled and implementing of iteration schemes. This renders their advantages over standard non-linear FEM modeling [7, 13-15] dubious and motivates seeking alternative, simpler analytical failure criteria applicable for evaluation of the residual CAI strength at a given extent of BVID.

It was noticed that, for sandwich coupons studied in the current project, an increase in dent depth usually precedes the onset of lateral growth of the dent. Therefore, as an alternative analytical criterion for imminent fracture, the compressive stress acting on the crushed honeycomb in flatwise direction at the center of the dent reaching the honeycomb crushing plateau stress can be considered.

A somewhat similar problem of finding the compressive stress σ in a facesheet with sinusoidal geometric imperfection that causes the interfacial normal stress between the facesheet and core to take the critical value σ_u , has been solved in [16] for isotropic facesheet with Young's modulus E_f :

$$\sigma = B_2 E_f^{1/3} E_c^{2/3} \quad (1)$$

where E_c is modulus of the isotropic core. The prefactor B_2 in Eq. (1) is expressed as

$$B_2 = \left(\frac{\rho^2 \theta^2}{12} + \frac{f(\theta)}{\rho} \right) (1 + k \theta^2 f(\theta))^{-1}. \quad (2)$$

The quantities entering Eq. (2) are given by the following expressions [16]:

$$\rho = \frac{h_f}{h_c} \left(\frac{E_f}{E_c} \right)^{\frac{1}{3}}, \quad (3)$$

$$\theta = \frac{\pi h_c}{l}, \quad (4)$$

$$f(\theta) = \frac{2}{\theta} \frac{(3 - \nu_c) \sinh \theta \cosh \theta + (1 + \nu_c) \theta}{(1 + \nu_c)(3 - \nu_c)^2 \sinh^2 \theta - (1 + \nu_c)^3 \theta^2}, \quad (5)$$

$$k = \frac{w_0}{h_c} \frac{E_c}{\sigma_u}, \quad (6)$$

where h_f and h_c denote facesheet and core thicknesses, the amplitude w_0 and half-wavelength of the sinusoidal initial imperfection are designated as l (see also the schematics in Fig. 4.1), respectively, ν_c is Poisson's ratio of the core, and σ_u stands for the ultimate normal stress acting in the facesheet/core interface. The form $f(\theta)$ given by Eq. (5) corresponds to a flat facesheet opposite to the sinusoidally perturbed one.

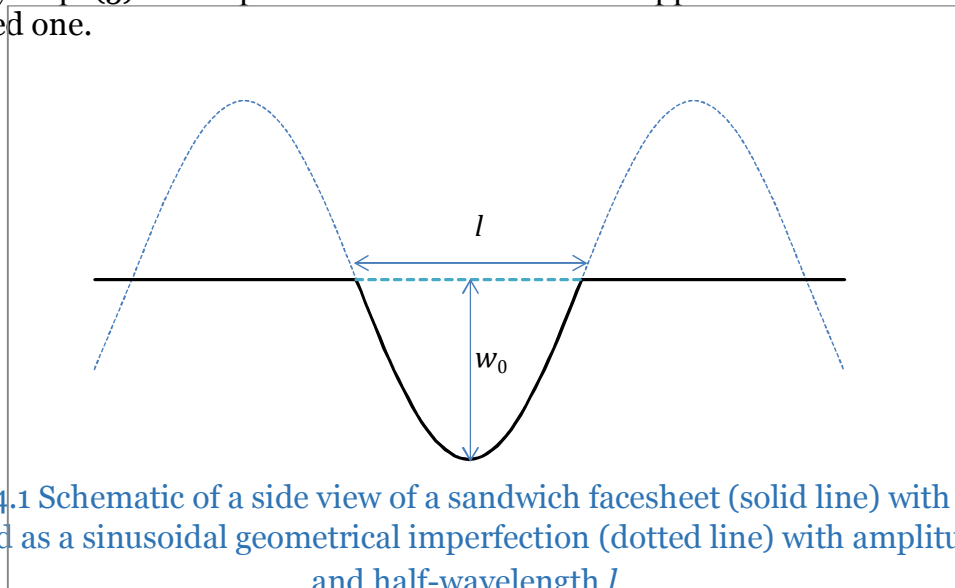


Figure 4.1 Schematic of a side view of a sandwich facesheet (solid line) with a dent modeled as a sinusoidal geometrical imperfection (dotted line) with amplitude w_0 and half-wavelength l .

As a rough approximation, we apply Eq. (1) for a BVID in a form of a dent, identifying the imperfection amplitude w_0 with dent depth and half-wavelength of imperfection l with dent diameter as shown schematically in Fig. 4.1. E_f for the

composite facesheet is taken as the modulus in CAI loading direction, E_c is flatwise compression modulus of the honeycomb core, and σ_u is equated to the flatwise crushing plateau stress of the honeycomb core. Since $f(\theta)$, according to Eq. (5), is only weakly dependent on ν_c , the value of 0.3 was assumed for ν_c .

Experimental CAI strength (i.e. critical facesheet stress) of the coupons from series ESA_027, ESA_028, and ESA_029 that failed by unstable dent propagation in CAI is plotted in Fig. 4.2 as a function of the critical skin stress predicted by Eq. (1) using the residual dent depth, w_0 , and diameter, l , values measured after the quasi-static or dynamic indentation tests. For these series, facesheet lay-up was [0/60/-60/0] and honeycomb core was 20 mm thick and had 6.4 mm cells. It is seen that Eq. (1) provides a conservative estimate of CAI strength.

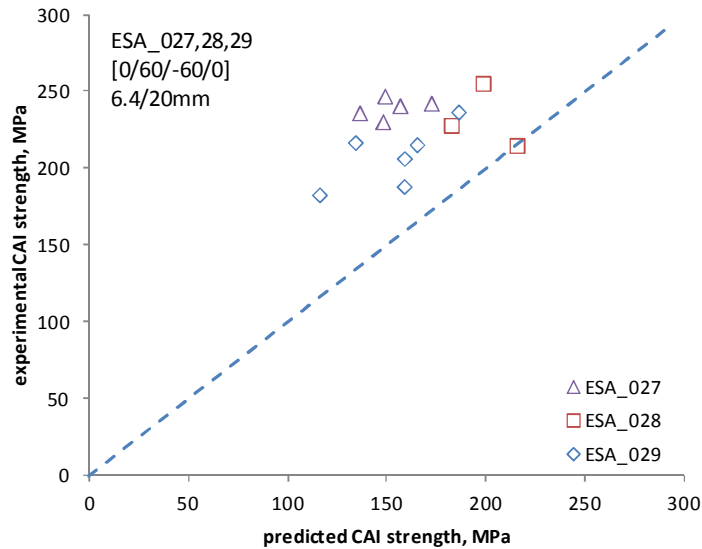


Figure 4.2 Experimental CAI strength of sandwich coupons having [0/60/-60/0] facesheet and 20 mm thick 6.4-mm-cell core as a function of the prediction by Eq. (1).

For coupons of series ESA_034 and ESA_035 having the same facesheet lay-up but thicker, 30 mm, core with 6.4-mm cells, the same conclusion on applicability of Eq. (1) for estimation of the lower bound on CAI strength can be made based on the strength data of coupons that failed by dent propagation, presented in Fig. 4.3. However, for the thinner facesheets with lay-ups [90/0] (ESA_039, 40) and [60/-60/0] (ESA_036), the predicted CAI strength is closer to the experimental values, and for some coupons of ESA_036 series the theoretical estimates become non-conservative, overestimating the experimentally determined strength by up to 15%.

Concerning the mode of CAI failure, coupons with [0/60/-60/0] and [60/-60/0] layup facesheets failed by propagation of a relatively wide and smooth dent. By contrast, the dents growing in [90/0] facesheet coupons were narrower and sharper, with signs of facesheet fracture by kinking/bending at the vertex of the dent.

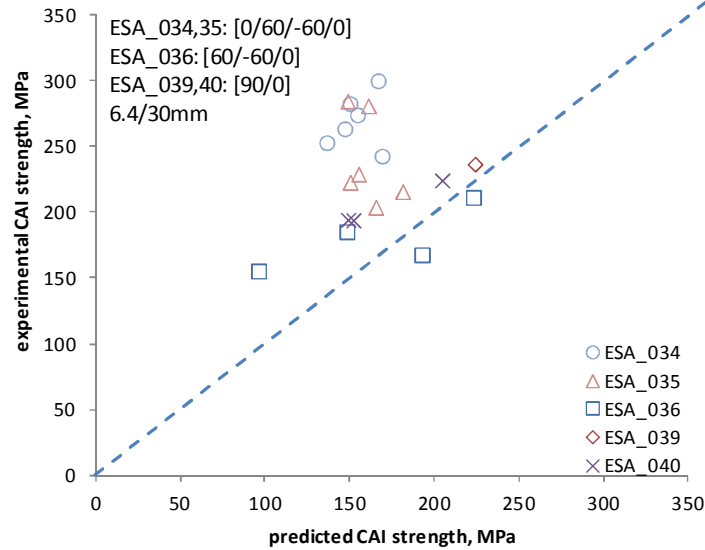


Figure 4.3. Experimental CAI strength of sandwich coupons having [0/60/-60/0], [60/-60/0], or [90/0] facesheets and 30 mm thick 6.4-mm-cell core as a function of the prediction by Eq. (1).

CAI strength for failure by unstable dent propagation, determined for the same range of facesheet lay-ups, but for coupons with stiffer honeycomb core of 3.2-mm cell size and 20 mm or 30 mm thickness, is shown in Fig. 4.4 for 20 mm thick and in Fig. 4.5 for 30 mm thick honeycomb core. It is seen that the critical CAI skin stress values are higher than those for 6.4-mm-cell core shown in Figs. 4.2 and 4.3.

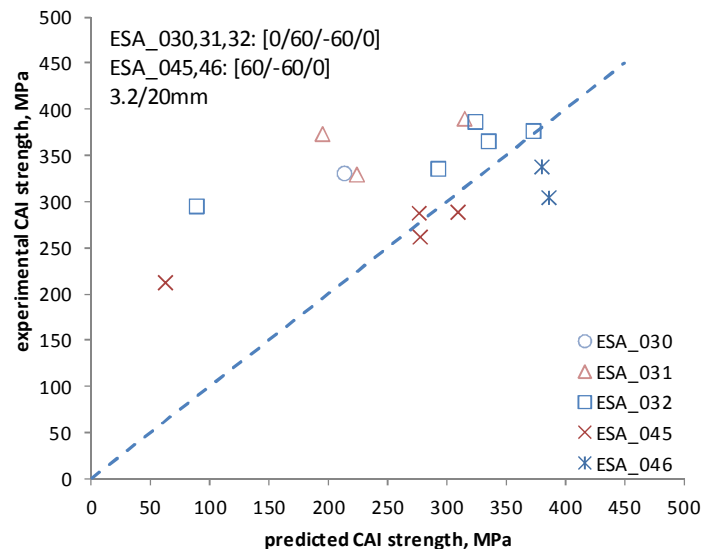


Figure 4.4. Experimental CAI strength of sandwich coupons having [0/60/-60/0] and [60/-60/0], facesheets and 20 mm thick 3.2-mm-cell core as a function of the prediction by Eq. (1).

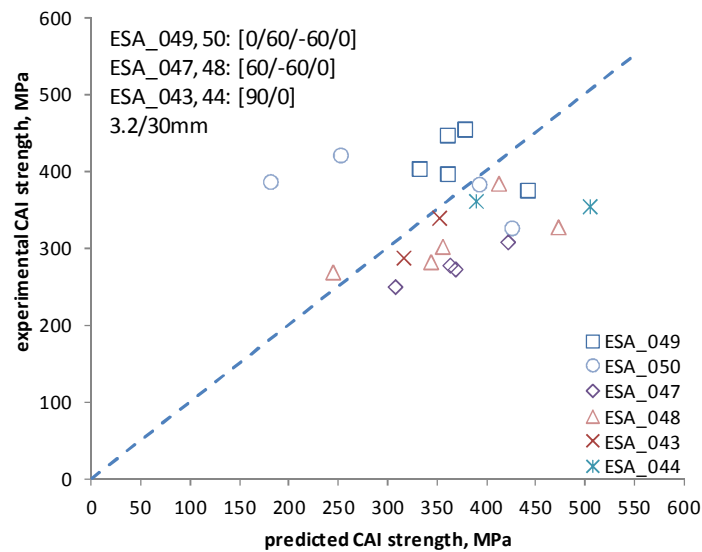


Figure 4.5 Experimental CAI strength of sandwich coupons having [0/60/-60/0], [60/-60/0], or [90/0] facesheets and 30 mm thick 3.2-mm-cell core as a function of the prediction by Eq. (1).

The theoretical estimate of CAI strength by Eq.(1) remains conservative for coupons with [0/60/-60/0] skins failing by dent propagation (ESA_030, 31, 32), Fig. 4.4. Notably, this is no longer true when coupons of the same lay-up start growing narrower dents and exhibiting some facesheet fractures at the vortex of the growing dent, (ESA_049, 50), Fig. 4.5. In this case, Eq.(1) yields only an estimate of average CAI strength, with some [0/60/-60/0]-skin coupons failing at smaller loads than predicted as can be seen in Fig. 4.5. The prediction becomes non-conservative for coupons with the thinner facesheets [60/-60/0] and [90/0]. This is apparently related to the differing dent geometry, propagating dents being sharper in these facesheet/core combinations than assumed in the model, Fig. 4.1. The predicted CAI strength in this case can exceed the experimental by up to 40% as suggested by Fig. 4.5.

As the current test series of indented sandwich coupons demonstrated, failure of part of them was not apparently related to the BVID. Therefore, presence of other pre-existing stress concentrators caused, e.g., by manufacturing or loading imperfections needs to be allowed for separately. The CIA strength data presented above in Figs. 4.2-4.5 relate only to coupons the failure of which initiated at the BVID location. The results obtained indicate that Eq. (1) yields a conservative estimate of CAI strength of a sandwich coupon with BVID only if the CAI failure mode is core crushing by longitudinal propagation of a wide smooth dent. Predicted CAI strength may become non-conservative if the sandwich failure mechanism involves growing of a sharp dent with facesheet failure. Nevertheless, the results obtained suggest that, at least for the sandwich coupons considered, Eq. (1) can be applied for a rough preliminary assessment of the effect of BVID of known dimensions on the residual CAI strength.

4.2 References

1. Hasseldine BPJ, Zehnder AT, Keating BD, Singh AK, Davidson BD. Compressive strength of aluminum honeycomb core sandwich panels with thick carbon–epoxy facesheets subjected to barely visible indentation damage. *Journal of Composite Materials* 2016, Vol. 50(3) 387–402.
2. Tomblin J, Lacy T, Smith B, Hooper S, Vizzini A, Lee S. Review of damage tolerance for composite sandwich airframe structures. Washington, DC: Federal Aviation Administration, Report No. DOT/FAA/AR-99/49, 1999.
3. Moody C, Vizzini A. Damage tolerance of composite sandwich structures. Washington, DC: Federal Aviation Administration, Report No. DOT/FAA/AR-99/91, 2000.
4. Lacy T, Samarah I, Tomblin J. Damage resistance characterization of sandwich composites using response surfaces. Washington, DC: Federal Aviation Administration, Report No. DOT/FAA/AR-01/71, 2002.
5. Shyprykevich P, Tomblin J, Ilcewicz L, Vizzini AJ, Lacy TE, Hwang Y. Guidelines for analysis, testing, and nondestructive inspection of impact damaged composite sandwich structures. Washington, DC: Federal Aviation Administration, Report No. DOT/FAA/AR-02/121, 2003.
6. Tomblin J, Raju K, Walker T, Acosta JF. Damage tolerance of composite sandwich airframe structures – additional results. Washington, DC: Federal Aviation Administration, Report No. DOT/FAA/AR-05/33, 2005.
7. Xie Z, Vizzini AJ, Yang M. On residual compressive strength prediction of composite sandwich panels after low-velocity impact damage. In: Thomsen OT, Bozhevolnaya E and Lyckegaard A (eds) *Sandwich structures 7: advancing with sandwich structures and materials*. The Netherlands: Springer, 2005, 363–372.
8. Ratcliffe J, Jackson W. A finite element analysis for predicting the residual compression strength of impact-damaged sandwich panels. Hampton, VA: National Aeronautics and Space Administration, Report No. NASA/TM-2008-215341, 2009.
9. Minguet PJ. A Model for Predicting the Behavior of Impact-Damaged Minimum Gage Sandwich Panels Under Compression. In: *32nd AIAA/ASME/ASCE/AHS/ASC Structures, Structural Dynamics and Materials Conference*, 1991, 1112-1122.
10. Moody RC, Vizzini AJ. Incorporation of a compliance change due to impact in the prediction of damage growth in sandwich panels, In: *Proceedings of the 13th International Conference on Composite Materials*, Beijing, China, 2001, 10 p.
11. Xie, Z, Vizzini AJ. A feasible methodology for engineering applications in damage tolerance of composite sandwich structures. *Journal of Composite Materials*, Vol. 38, No. 11, 2004, 891-914.

12. Xie Z, Vizzini AJ. Damage Propagation in a Composite Sandwich Panel Subjected to Increasing Uniaxial Compression after Low-velocity Impact. *Journal of Sandwich Structures & Materials* 2005;7: 269-288.
13. Xie Z, Vizzini AJ, Tang Q. On residual compressive strength prediction of composite sandwich panels after low-velocity impact damage. *Acta Mechanica Solida Sinica*, Vol. 19, No. 1, March, 2006, 9-17.
14. Hwang Y, Lacy TE. Numerical estimates of the compressive strength of impact-damaged sandwich composites. *Journal of Composite Materials*, Vol. 41, No. 3, 2007, 367-388.
15. Castanié B, Aminanda Y, Bouvet C, Barrau J-J. Core crush criterion to determine the strength of sandwich composite structures subjected to compression after impact. *Composite Structures* 86 (2008) 243–250.
16. Allen HG. Chapter 8 - Wrinkling and other forms of local instability. In: *Analysis and Design of Structural Sandwich Panels*. Pergamon Press, 1969, pp. 156–189.

5 Guidelines for experimental investigations

In general guidelines of testing practices can be observed from two aspects: best practices of specimen manufacturing and best practices of experimental investigations (for both coupon level and panel level).

Material characterisation of the face sheets should be carried out for plates manufactured by the same technology that will be used for manufacturing of sandwich skin plates, ensuring that variability in factors affecting material properties, such as: fiber/matrix volume ratio, void contents etc., are minimized or excluded at all. Current, as well as similar studies, showed that strain measurement by strain gages produce most accurate measurements compared to digital image correlation, clip-on strain extensometers or any other strain/deformation measurement devices. Depending on the number of coupon specimens and availability of strain gages, partial instrumentation with strain gages in combination with DIC can be used, provided that DIC measurements are consistent and can be useful.

The same assumptions can be applied to adhesive coupon tests. Caution should be made to proper adhesive mixing and degassing to form void free cross section of specimens for tension/compression tests. Adhesive specimens manufactured for material characterisation contained certain amount of voids in form of gas bubbles across the cross section, Fig. 5.1, which affected proper material properties by reducing effective cross section area. Adhesive properties obtained by peel drum test corresponds to Mode I crack propagation and can be successfully implemented in finite element analyses as skin/honeycomb debonding propagation properties.

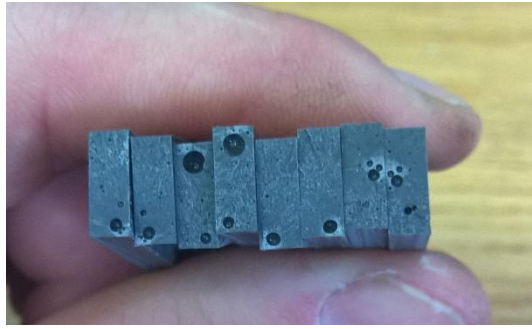


Figure 5.1 Gas bubbles in adhesive resin coupon specimens.

Material characterisation of the honeycomb will remain questionable due to aspects, that it is hard to measure real honeycomb foil thickness (foil thickness 0.0178 mm) with appropriate precision, by available measurement devices. Foil thickness taken according to manufacturer specs. The same can be applicable to mechanical properties of aluminium alloy used. Stiffness as well as strength and plasticity behaviour should be assumed for material matching as close as possible to original, in case if honeycomb manufacturer doesn't provide all the data. Mechanical properties of plastic deformation of stabilized honeycomb structure can be extracted from carefully prepared flatwise compression-tension test as well as in-plane shear test. The major outcome of flatwise compression test are honeycomb buckling (σ_B) and crushing stress (σ_{CR}) in combination with accompanying (E_{core}) modulus and (E_{tan}) tangent modulus, which was used in finite element model for honeycomb structure material representation based on experimentally measured values.

Depending on available technology of composite face sheet manufacturing, well compacted (low void, appropriate fiber/matrix ratio) composite skin of desired composition, should be manufactured (preferably) as a one-piece lay-up, forming uniform thickness plate (if implemented technology allow), capable to produce batch (atleast 6) of specimens (150 mm x 100 mm) with both face skins made off one plate. This assures that both sides of the specimen can be qualified for impact and there is no thickness imbalance for compression test (equalized load distribution). Composite skin manufacturing technology available at the current study, was not able to produce large enough plates, having only one even surface and uneven thickness distribution toward the edges of the panel, see Fig. 5.2, caused by loss of matrix during curing process. This aspect can lead to inappropriate skin/honeycomb adhesion, taking into account, that even surfaces were placed as outside surfaces of the assembled panel. Panel assembly technique used (panels were assembled between two rigid glass plates), produced panels with constant height, where honeycomb core was in contact with skin at the panel central part, but having gaps on panel edges (there was not actual gaps between honeycomb and skin were detected, but rather skin and honeycomb gap was filled with resin). Since panel was cut in half, forming two rows of specimens (2 x 3), Fig. 5.3, one side of each specimen has proper honeycomb to skin connection but other side has (potentially !!!) lower stiffness connection (outer side). Difference in stiffness of connection of honeycomb and skin material can lead to improper load distribution along the panel width, Fig. 5.4, 5.5, or skin debonding due to pulling out of the honeycomb foil from the adhesive, due to small adhesion surface. To reduce this factor, larger skin plates

must be manufactured, to allow to cut more material at the panel side edges, if those are affected by resin flow.

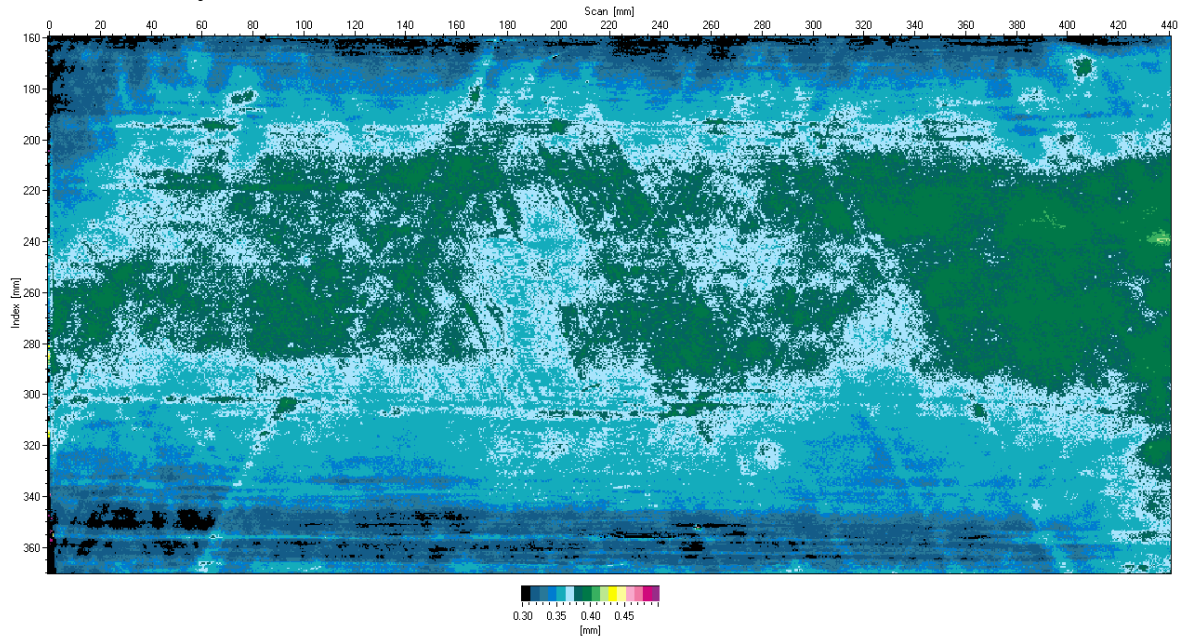


Figure 5.2 US scan of thickness distribution along the skin panel.



Figure 5.3 Panel cut to individual specimens.

Impact testing of panel specimens showed higher scatter in terms of maximum indentation value and repeatability. This as well as quazi-static loading by load control were used at earlier stages of the current study proved to produce hard to repeat cases in which similar loading conditions led to completely different amount of residual damage due to variation of panel stiffness across the series of specimens. This aspect led to the use of displacement controlled loading, which is not as highly affected by panel stiffness variation, as for load controlled. Series of experimental tests at the end of the project includes mostly displacement controlled loading, accompanied with some impact tested. For cases involving low intensity indentation there are good repeatability observed, while in cases of sever

indentation, related with certain amount of composite skin damage some specimen can be punctured by spring-back effect of panel bending, while others not.



Figure 5.4 Strain distribution measurement along the panel width.

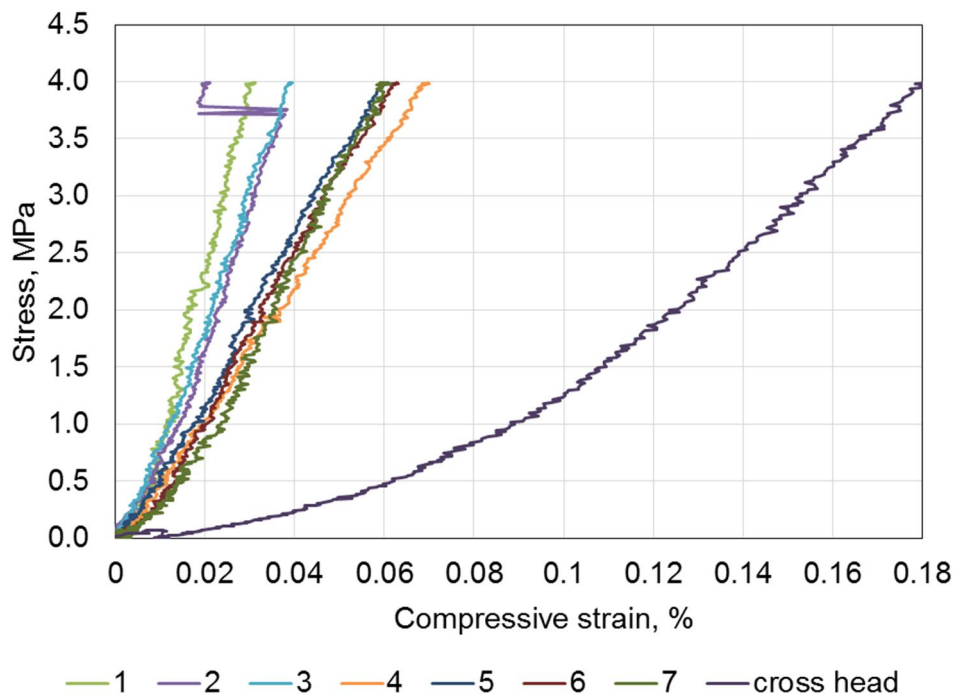


Figure 5.5 Measured strain distribution along the panel width.

Edgewise compression of the panels (CAI) showed that applicability of the ASTM D7137 proposed test fixture designed for compression after impact tests of

comparatively thick laminated plates, doesn't work for sandwich structures with thin skins. Early attempts to test sandwich specimens in this fixture lead to composite edge rupture at the contact interface with loading end plates. Some related studies referencing to the use of free side edgewise compression according to ASTM C364. Both loaded edges were casted in some kind of resin-filler mixture of depth of the order of sandwich thickness. Edgewise compression tests were carried out on the simple flat compression platens with one end rested on spherical seat. Caution should be taken to the edge casting quality, to form as precise as possible plane to avoid load concentration on panel edges or in the middle of the panel, depending on curvature of end plane. Early experiments carried out during the current study showed that improperly designed casting rigs, caused non-planar panel edges, see Fig. 5.6. Majority of the specimens suffered by overloaded panel edges, resulting in skin debonding failure over indentation triggered. Poorly mixed or improperly cured resin casting or weak adhesion (poor surface treatment) to carbon fiber skins will lead to debonding of the skin inside the casting block and skin composite edge crushing against the compression platens.

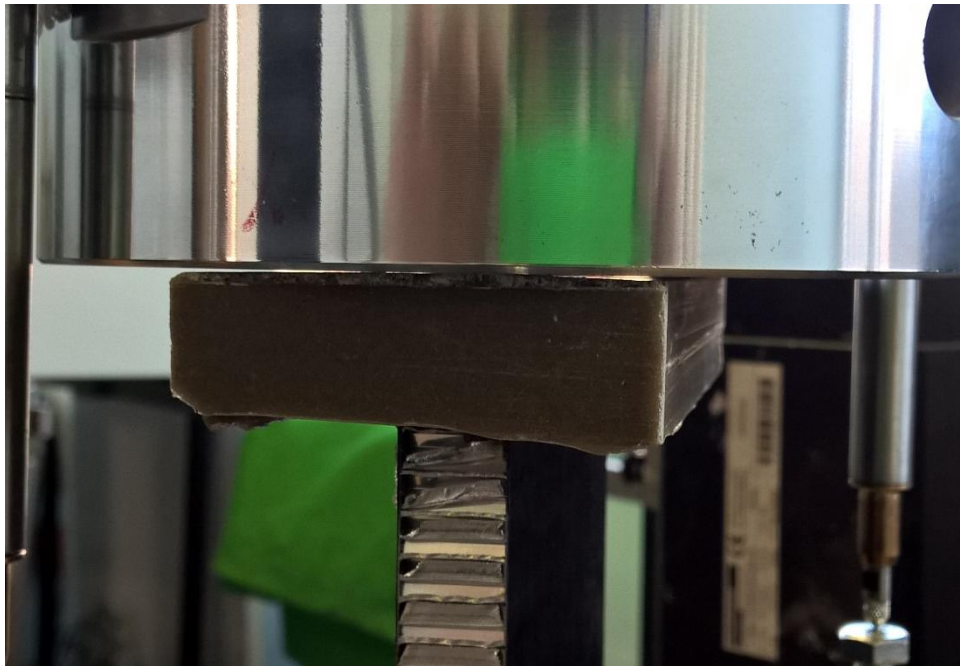


Figure 5.6 Specimen ends with non-planar edges.

6 Conclusions

The current report highlight the numerical simulation and prototyping guidelines. Each chapter is focused on specific aspects of damage assessment process, starting with damage introduction to compression resistance of investigated panels. Eventhough it would be extreamly beneficiarly to have a simple and short rule`s of thumb derived, nevertheless a background knowledge and set-up notes are very important details for efficient numerical simulations. Essential tips are given in each chapter, therefore reader is advised to learn background settings in order to implement guiding principles for both numerical and experimental work.

As a best practice a dozen of validation cases have been elaborated and alrady available on project web page under tool section: http://bnm4eks.rtu.lv/tools_en.html this serves as a benchmarking database so important for seting up and validating the numerical procedure.